arXiv:1610.01678v3 [physics.flu-dyn] 13 Nov 2017

Giant deviation of a relaxation time from generalized Newtonian theory in Discontinuous Shear Thickening suspensions

Rijan Maharjan and Eric Brown
Department of Mechanical Engineering and Materials Science, Yale University, New Haven, CT 06520
(Dated: March 9, 2022)

We investigated the transient relaxation of a Discontinuous Shear Thickening (DST) suspension of cornstarch in water. We performed 2 types of relaxation experiments starting from a steady shear in a parallel plate rheometer, followed by either stopping the top plate rotation and measuring the transient torque relaxation, or removing the torque on the plate and measuring the transient rotation of the tool. We found that at low effective weight fraction $\phi_{eff} < 58.8 \pm 0.4\%$, the suspensions exhibited a relaxation behavior consistent with a generalized Newtonian fluid in which the relaxation is determined by the steady-state relationship between shear stress and shear rate. However, for larger weight fraction $58.8\% < \phi_{eff} < 61.0\%$, near the liquid-solid transition $\phi_c = 61.0 \pm 0.7\%$, we found relaxation behaviors qualitatively and quantitatively different from the generalized Newtonian model. The regime where the relaxation was inconsistent with the generalized Newtonian model was the same where we found positive normal stress during relaxation, and in some cases we found an oscillatory response, suggestive of a solid-like structure consisting of a system-spanning contact network of particles. This regime also corresponds to the same packing fraction range where we consistently found discontinuous shear thickening in rate-controlled, steady-state measurements. The relaxation time in this range scales with the inverse of the critical shear rate at the onset of shear thickening, which may correspond to a contact relaxation time for nearby particles in the structure to flow away from each other. In this range the relaxation time was the same in both stress- and rate-controlled relaxation experiments, indicating the relaxation time is more intrinsic than an effective viscosity in this range, and is needed in addition to the steady-state viscosity function to describe transient flows. The discrepancy between the measured relaxation times and the generalized Newtonian prediction was found to be as large as 4 orders of magnitude, and extrapolations diverge in the limit as $\phi_{eff} \to \phi_c$ as the generalized Newtonian prediction approaches 0. This quantitative discrepancy indicates the relaxation is not controlled by the dissipative terms in the constitutive relation. At the highest weight fractions, the relaxation time scales were measured to be on the order of $\sim$ 1 s. The fact that this timescale is resolvable by the naked eye may be important to understanding some of the dynamic phenomenon commonly observed in cornstarch and water suspensions. We also showed that using the critical shear rate $\dot{\gamma}_c$ at the onset of shear thickening to characterize the effective weight fraction ϕ_{eff} can more precisely characterize material properties near the critical point ϕ_c, allowing us to resolve this transition so close to ϕ_c. This conversion to ϕ_{eff} can also be used to compare experiments done in other laboratories or under different temperature and humidity conditions on a consistent ϕ_{eff} scale at our reference temperature and humidity environment.

PACS numbers: 47.50.-d, 83.60.Rs, 47.57.E-, 83.80.Hj

Discontinuous Shear Thickening (DST) suspensions are known to exhibit a number of transient phenomena which are associated with the ability to form a temporary solid-like jammed state in response to shear. Such phenomena include an impact response strong enough to be used in commercial impact protection devices [1, 2], a shear resistance strong enough to break or jam industrial mixing equipment [3], the ability of people to run on the surface of cornstarch and water [4, 5], the formation of stable holes in the surface of a vertically vibrated layer of the fluid [6], and oscillations in the velocity of a sphere sinking in the fluid [7]. There is also an unjamming process for each of these phenomena, in which the solid-like state relaxes back to a fluid-like state, which determines how long the phenomena last and may be relevant for cyclic motion. Our goal is to characterize the transient relaxation component of the rheology of DST suspensions to better understand such phenomena.

Traditionally, shear thickening is defined by an increase in effective viscosity η with increasing shear rate $\dot{\gamma}$ or shear stress τ, where $\eta = \tau/\dot{\gamma}$ in a steady-state flow in a rheometer. In many concentrated suspensions such as cornstarch and water, this effect can be so strong that the increase of η or τ in $\dot{\gamma}$ can be 1-3 orders of magnitude, and can even appear to be discontinuous in $\dot{\gamma}$ at a critical shear rate $\dot{\gamma}_c$. The steepness of $\tau(\dot{\gamma})$ tends to increase with packing fraction up to the liquid-solid transition ϕ_c, above which shear thickening is no longer observed [8, 9], so shear thickening is most prominent just below ϕ_c (see [3, 5, 10] for reviews on shear thickening).

A typical purpose of rheology measurements is to obtain a constitutive relation for the shear stress which could then be inserted into a modified Navier-Stokes equation in place of the usual shear stress term, and solved to describe flows under different conditions (i.e. geometries, boundary conditions, and transients). However, transient impact experiments have revealed a very different rheology than the steady-state $\tau(\dot{\gamma})$ from

rheometer experiments described in the previous paragraph. For example, under impact DST suspensions support stresses orders of magnitude larger than inferred from steady-state rheometer measurements [11–13]. This contradicts the simplest rheological model of a generalized Newtonian fluid – meaning the same constitutive relation $\tau(\dot{\gamma})$ that has a single value of shear stress τ at each shear rate $\dot{\gamma}$ applies to all flows. Thus, any complete rheology that includes both the steady-state and transient behavior of DST suspensions requires more information than just $\tau(\dot{\gamma})$.

Another unusual phenomena of DST fluids is the formation of stable holes in the surface of a vertically vibrated layer of the fluid [6]. It has been shown that these structures cannot be stable due to a rheology described by any generalized Newtonian function of the form $\tau(\dot{\gamma})$ – regardless of whether the function includes shear thickening. Instead the $\tau(\dot{\gamma})$ must have a hysteresis such that there is a difference in stress on the up- and down-cycles of the vibration to overcome the gravitational and surface tension forces that are trying to close the hole [14].

A third unusual phenomena of DST fluids is that a sphere sinking in the fluid has an oscillating velocity, rather than monotonically approaching a terminal velocity [7]. It was shown that this also cannot be described with any generalized Newtonian function $\tau(\dot{\gamma})$, rather it can also be described in principle by hysteresis in $\tau(\dot{\gamma})$ [7, 15].

Making use of this knowledge that hysteresis in $\tau(\dot{\gamma})$ is required to explain transient and dynamic phenomena of DST fluids, a simple phenomenological model was proposed by Ozgen et al. [16]. It consists of a $\tau(\dot{\gamma})$ relationship with an effective viscosity that increases with shear rate to mimic shear thickening. This term was made to have hysteresis in $\tau(\dot{\gamma})$ such that it depends not only on the instantaneous shear rate, but on a weighted average of shear rate over a preceding time interval, corresponding physically to a time delayed response before the strong solid-like response to impact, as well as a relaxation time over which the effective viscosity decays after the shear rate decreases. This model was able to qualitatively reproduce the phenomena that were previously argued to require hysteresis; the stable holes in a vibrated layer, and oscillations in the velocity of a sinking sphere. The model also reproduced some phenomena that are known to occur in DST fluids, but have not been explained previously; in particular the abilities of a sphere to bounce and roll on the surface of the suspension [17]. This success is remarkable in that no simulation has been able to produce any one of these phenomenon before – even individually – yet several were produced at once with this model. However, this model was made before any of the relevant rheological parameters were measured for real materials, so the parameters were freely tuned to reproduce these phenomena.

Despite the popular interest in these transient and dynamic phenomena, it is remarkable that there has been little systematic study of transient rheology that goes beyond the traditional steady-state $\tau(\dot{\gamma})$ function for DST suspensions. Oscillatory rheology is often used to characterize time-dependence in the constitutive relation. Typically these results supported the steady shear rheology description [18, 19], but in general these oscillatory measurement have not revealed a different relaxation behavior or any additional features of a constitutive relation that would help explain any transient phenomena. There have been some measurements identifying hysteresis when the control parameter is ramped quickly [14, 20], but not detailed enough to expand on the constitutive relation. Measurements of the delay in stress response after impact identified by Ozgen et al. [16] have only recently been reported in another paper by us [13]. The other time-dependent behavior that could result in hysteresis in $\tau(\dot{\gamma})$ in combination with the delay before the solid-like like response is the relaxation of the solid-like state [16]. While a relaxation of stress to a steady-state behavior has been observed previously [21], analysis of this transient, or any trends in control parameters such as packing fraction, have not been reported.

In this paper, we characterize the relaxation behavior in rheometer experiments. To systematically characterize a relaxation behavior we report time series of the relaxation of stress or shear rate over time after a flow is stopped or stress removed, respectively. It remains to be seen over what range of packing fractions the relaxation behavior can be described by a generalized Newtonian model, and if other relaxation behaviors are observed which might help explain some of the unusual phenomena observed in DST suspensions, so we report measurements as a function of packing fractions near the liquid-solid transition where shear thickening behavior is strongest [8, 9]. It is expected that this relaxation data will be an essential element in constitutive models of transient and dynamic phenomena such as proposed by Ozgen et al. [16].

The remainder of this paper is organized as follows. We describe the materials and general methods used in Secs. I and II, respectively. In Sec. III we show typical steady-state viscosity curves for suspensions of cornstarch and water from which we obtain parameter values to compare to transient measurements. In Sec. IV we present a method to more precisely characterize the effective weight fraction, which is helpful for resolving trends in relaxation behavior near the liquid-solid transition. In Sec. V, we report time series of the relaxation of stress and shear rate over time. We identify the different qualitative types of relaxation observed in stress-controlled experiments at different weight fraction ranges and compare them to a generalized Newtonian model in Secs. V A-V C. We compare effective viscosities from transient and steady state measurements in Sec. V D. To compare to relaxation in a different type of flow, we report measurements of shear-rate-controlled relaxation behavior in Secs. V E-V G. In Sec. V H, we compare the measured relaxation times between stress- and rate-controlled measurements. In Sec. VI, we com-

pare the results of different sections, and develop a self-consistent explanation of the relaxation behavior in the range where the relaxation is inconsistent with the generalized Newtonian model.

I. MATERIALS

Cornstarch was purchased from *Carolina Biological Supply* and suspended in tap water, to obtain a typical DST fluid [5]. The samples were created at a temperature of 22.0±0.6 °C and humidity of 48±6%, where the uncertainties represent day-to-day variations in the respective values. A four-point scale was used to measure quantities of cornstarch and water to obtain a weight fraction ϕ_{wt}. While a weight fraction by volume is more traditional, obtaining the weight fraction by volume requires knowing the water content (which depends on temperature and humidity) and porosity of the cornstarch – both of which are difficult to obtain [5]. As a result of this difficulty, volume or weight fraction measurements made in different laboratories or different seasons with different environmental conditions are generally not comparable, but still useful as a quantitative control parameter within data series from the same lab and season. Since a volume or weight fraction that could be compared in different laboratories is desirable, we introduce a method in Sec. IV to identify an effective weight fraction scale that can be compared from lab to lab and season to season.

Each suspension was mixed until no dry powder was observed. The sample was further shaken in a *Scientific Instruments Vortex Genie 2* for 30 seconds to 1 minute on approximately 60% of its maximum power output. We directly measured a density of 1200 ± 20 kg/m^3 for a suspension at $\phi_{wt} = 57\%$ based on the volume and weight in a graduated cylinder. If we extrapolate based on the fraction of cornstarch and water using the known density of water, this same value is consistent with the density for suspensions within the uncertainty for weight fractions from 51% to 63%, covering our entire measurement range.

II. METHODS

Suspensions were measured in an *Anton Paar MCR 302* rheometer in a parallel plate setup. The rheometer measured the torque M on the top plate and angular rotation rate ω of the top plate. In different experiments, either torque or rotation rate could be controlled, while the other was measured as a response. Flows of DST suspensions in such setups are neither uniform nor constant, exhibiting variations in the measured parameter in both space and time, with fluctuations as large as an order of magnitude larger than the mean over timescales of about 1 second [22]. Nonetheless, we can reproducibly characterize each steady state flow by the mean shear stress and shear rate [20]. The mean shear stress is given by $\tau = 2M/\pi R^3$ where R is the radius of the sample. While the mean shear rate varies along the radius of the suspension, the mean shear rate at the edge of the plate is used as a reference parameter, which is given by $\dot{\gamma} = R\omega/d$ where d is the gap height between the plates. The viscosity of the sample is measured as $\eta = \tau/\dot{\gamma}$ in a steady state. We also measured the force F on the top plate of the rheometer (upward positive) and report the mean normal stress $\tau_N = F/(\pi R^2)$. To calibrate the normal stress, we subtract the value obtained in steady-state measurements in the limit of zero shear rate. The gap height was usually set to $d = 1.25$ mm unless otherwise noted, and allowed to vary by 0.05 mm from experiment to experiment in an attempt to reduce the uncertainty on the sample radius. The sample radius was $R = 25.0 \pm 0.5$ mm, which results in an 8% error in the calculated shear stress τ when the plate radius R is used in calculations. The experiments were performed at a plate temperature of 23.5 ± 0.5 °C. A solvent trap was used to slow down the moisture exchange between the sample and the atmosphere. The solvent trap effectively placed a water seal around the sample, with a lipped lid around the sample and the lips touching a small amount of water contained on the top, cupped, surface of the tool.

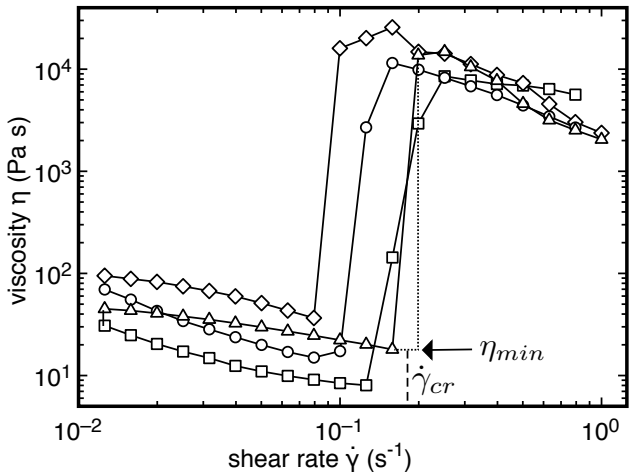


FIG. 1. An example of repeated ramps of steady-state viscosity η vs. shear rate $\dot{\gamma}$ for cornstarch and water at weight fraction $\phi_{wt} = 59.6\%$. The symbols correspond to different ramps of increasing $\dot{\gamma}$ (squares, diamonds) and decreasing $\dot{\gamma}$ (triangles, circles). The critical shear rate $\dot{\gamma}_c$ and minimum viscosity η_{min} are obtained at the onset of shear thickening for each curve.

III. STEADY STATE VISCOSITY CURVES

While steady-state viscosity curves have been characterized previously [3, 5, 10], we present them here for comparison to relaxation measurements in the same samples in later sections. To obtain steady-state viscosity curves, each sample was pre-sheared to produce a state

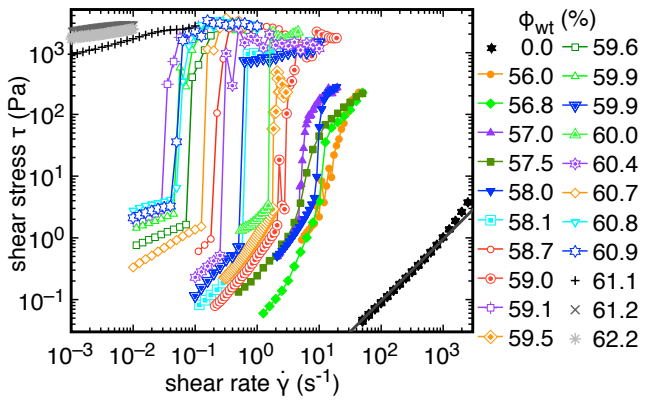


FIG. 2. (color online) Shear stress τ as a function of shear rate $\dot{\gamma}$ at different weight fractions ϕ_{wt} shown in the key. For $58.1\% \leq \phi_{wt} < \phi_c = 61.0\%$, discontinuous shear thickening is seen as a sharp jump in stress. For $56.0\% \leq \phi_{wt} \leq 58.0\%$, we find continuous shear thickening.

independent of the sample loading history. We used a linear ramp in shear rate over 200 seconds, covering a shear rate range that crosses the shear thickening regime and a net shear strain greater than 100%. The shear rate was then ramped down then back up twice with a constant rate of variation on a logarithmic scale, with 10 data points per decade and data averaged for 50 seconds per point.

Figure 1 shows an example of the steady state viscosity η as a function of shear rate $\dot{\gamma}$ for the four ramps after the preshear at ϕ_{wt}=59.6%. There is a large run-to-run variation even for the same sample in a constant environment that seems to be a natural variation; the standard deviation of the 4 ramps is 30%, as is typical in measurements of cornstarch and water [20]. We observed no significant systematic trend in the repeated ramps, confirming the pre-shear eliminated any effects of loading history, environmental change, or any other systematic effects during measurement of a single sample.

Averages of the shear stress τ as a function of shear rate $\dot{\gamma}$ over the 4 ramps are shown in Fig. 2 for different weight fractions ϕ_{wt}. At each weight fraction in the range $58.1\% \leq \phi_{wt} < 61.0\%$, a discontinuous jump in $\tau(\dot{\gamma})$ can be seen from τ_{min} ($\sim 10^0$ Pa) to τ_{max} ($\sim 10^3$ Pa), corresponding to discontinuous shear thickening. In these cases, the jump in shear stress between adjacent points in shear rate was between 1-3 orders of magnitude for each curve. For $56.0\% \leq \phi_{wt} \leq 58.0\%$, some of the repetitions had apparently discontinuous $\tau(\dot{\gamma})$ curves, with jumps in shear stress between adjacent points by a factor of 5-10, while others have a more gradual increase, resulting in average curves that are steep, but not discontinuous. Thus, we can define a transition between continuous and discontinuous shear thickening in rate-controlled experiments at ϕ_{wt} between 58.0% and 58.1%.

At higher weight fractions of $\phi_{wt} > 61.0\%$, we observed a yield stress on the order of 10^3 Pa in Fig. 2. We identified this liquid-solid transition $\phi_c = 61.0\%$ (also called the jamming transition). We did not observe shear thickening at weight fractions above ϕ_c because of the large yield stress [8, 9].

In all of these cases we present for suspensions, the Reynolds Number $Re = \rho d^2\dot{\gamma}/\eta < 1$ over the entire shear thickening range. Hence, inertial displacement does not contribute significantly to energy dissipation, and the corresponding dissipative force (proportional to velocity squared) is negligible in relaxation experiments starting from any of these steady states.

IV. CHARACTERIZING A MORE PRECISE EFFECTIVE WEIGHT FRACTION NEAR THE CRITICAL POINT

For a generalized Newtonian fluid, the energy dissipation rate, and thus the rate of relaxation is expected to scale with the viscosity (explained in Sec. V A), which diverges as it approaches the critical point at weight fraction ϕ_c [8, 9]. If we want to test this scaling close to the critical point, there is a resolution limit due to the uncertainty in the weight fraction of typically 1-2% in most measurements of suspensions. This uncertainty is due in part to the variability of the weight fraction with temperature and humidity because cornstarch adsorbs water from the atmosphere [20], and uncertainties introduced in the process of loading the sample onto the rheometer from an inhomogeneous sample. This can lead to large changes in the measured viscosity in repetitions of experiments from day-to-day and from lab-to-lab, with infinite sensitivity to the uncertainty in weight fraction due to the divergence of the viscosity at a nearby critical weight fraction ϕ_c [8, 9]. For example, while the critical shear rate $\dot{\gamma}_c$ at the onset of shear thickening (i.e. minimum shear rate of the shear thickening range) tends to decrease with weight fraction, in Fig. 2 we can find counterexamples such as $\phi_{wt} = 60.9\%$ and $\phi_{wt} = 60.4\%$ with an order of magnitude increase in $\dot{\gamma}_c$ when the apparent weight fraction increases by 0.5% when ϕ_{wt} is within 1% of ϕ_c.

This resolution limit can be circumvented, and scalings tested closer to the critical point, by instead characterizing the material in terms of a measurable property that diverges at ϕ_c, as errors in the diverging quantity will result in much smaller errors in weight fraction. Two such properties include the minimum viscosity η_{min} and the inverse of the critical shear rate $\dot{\gamma}_c^{-1}$, both measured at the onset of shear thickening [8, 23]. Thus, in order to obtain a more reliable measure of effective weight fraction near the critical point, we measure these values for each ϕ_{wt} to use as references for an effective weight fraction ϕ_{eff} that is more accurate in identifying the sample than ϕ_{wt}.

We identify the critical shear rate $\dot{\gamma}_c$ and viscosity at the onset of shear thickening η_{min} from the viscosity curves in Fig. 2. We averaged values of $\dot{\gamma}$ over the point

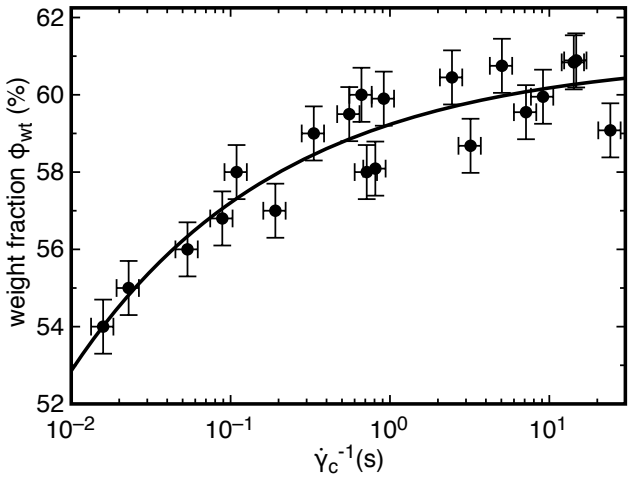


FIG. 3. Directly measured weight fraction ϕ_{wt} as function of inverse critical shear rate $\dot{\gamma}_c^{-1}$. A fit yields a conversion function $\phi_{eff} = -1.8\%\dot{\gamma}_c^{0.33}+61.0\%$, which can be used to identify an effective weight fraction ϕ_{eff} based on the measured parameter $\dot{\gamma}_c$, which is useful for precise characterizations near the critical weight fraction $\phi_c = 61.0\%$.

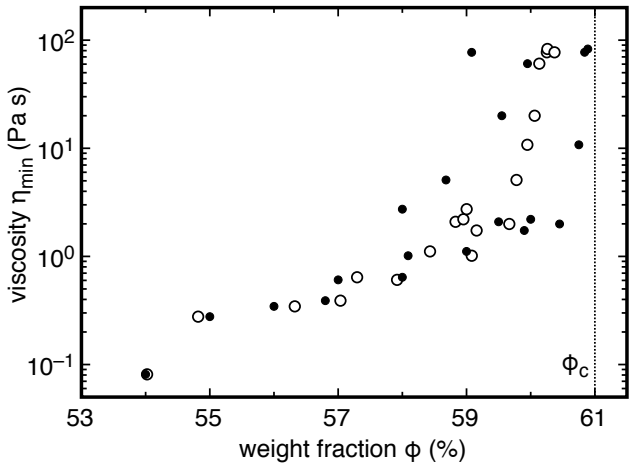


FIG. 4. Onset viscosity η_{min}. Solid symbols: as a function of the directly measured weight fraction ϕ_{wt}. Open symbols: as a function of the effective weight fraction ϕ_{eff} obtained from the fit of $\dot{\gamma}_c^{-1}$ in Fig. 3. Using the effective weight fraction ϕ_{eff} results in less scatter, allowing more precise characterization of trends in measured parameters near the critical point.

just before and the point just after the jump shown for example in Fig. 1 for each ramp, then further averaged over the 4 ramps. The viscosity at the lower end of the shear thickening range η_{min} was obtained by taking the η value just before each jump, then averaging over the four ramps. For both $\dot{\gamma}_c$ and η_{min} the run-to-run variation can be characterized by the standard deviation of the values from the four ramps. In following plots we use the standard deviation of the mean as the error when fitting mean values in each case, which are on average 16% for $\dot{\gamma}_c$ and 30% for η_{min}. We choose to use $\dot{\gamma}_c^{-1}$ as a reference parameter, having the smaller run-to-run variation of the two options.

To obtain a conversion to effective weight fraction ϕ_{eff}, we plot the directly measured ϕ_{wt} as a function of $\dot{\gamma}_c^{-1}$ for data at different weight fractions in Fig. 3. The conversion is obtained by least squares fitting a power law $\phi_{wt} = A\dot{\gamma}_c^B + \phi_c$ to the data with fixed $\phi_c = 61.0\%$ and fit parameters A and B. We use the 16% standard deviation of the mean in $\dot{\gamma}_c$ as an input error. We also adjust errors in ϕ_{wt} to a constant value of 0.7% to obtain a reduced $\chi^2 = 1$. The input error of 0.7% indicates a combination of the sample-to-sample uncertainty on weight fraction for our measurements plus any deviation of the fit function from the 'true' function describing the data. The fit yields $A = -1.8\pm0.2$ and $B = 0.33\pm0.03$, corresponding to the conversion function

$$\phi_{eff} = -1.8\%\dot{\gamma}_c^{0.33} + 61.0\% \ . \qquad (1)$$

with $\dot{\gamma}_c$ in units of s^{-1}. If we instead additionally fit the value of ϕ_c, then we obtain $\phi_c = 60.8 \pm 0.6$, consistent with the value obtained from yield stress measurements for the same data set, and the same uncertainty on weight fraction up to one point in the last digit [8].

With this conversion function, we can now calculate an effective weight fraction ϕ_{eff} from a measured $\dot{\gamma}_c$ with higher resolution than direct weight fraction measurements. The value of ϕ_{eff} using Eq. 1 corresponds to the value of the weight fraction in our reference temperature and humidity environment.

To test the usefulness of this effective weight fraction ϕ_{eff}, values of the onset viscosity η_{min} from the same measurements as data in Fig. 3 are plotted in Fig. 4 for different directly measured weight fractions ϕ_{wt}. Near ϕ_c, the data is very scattered as expected due to the error on the x-axis, making it difficult to track the expected divergence in weight fraction. For comparison, values of η_{min} are plotted in the same figure as a function of ϕ_{eff} using Eq. 1 to get ϕ_{eff} from the measured $\dot{\gamma}_c$ at each weight fraction. It can be seen that there is much less scatter in the data in terms of effective weight fraction ϕ_{eff} near ϕ_c. A power law fit of $\phi_{eff}(\eta_{min})$ analogous to Eq. 1 with the 30% standard deviation of the mean error on η_{min} requires a 0.3% error on ϕ_{eff} to obtain a reduced $\chi^2 = 1$. This smaller 0.3% error on ϕ_{eff} than the 0.7% error on ϕ_{wt} confirms that the ϕ_{eff} scale based on the fit of Eq. 1 more precisely relates to mechanical properties that diverge near ϕ_c (i.e. η_{min} and $\dot{\gamma}_c^{-1}$) than direct weight fraction ϕ_{wt} measurements.

V. RELAXATION

A. Relaxation of a generalized Newtonian fluid

To measure relaxation times, we performed transient experiments. We first applied a constant torque to the top plate until the flow reached steady-state, then re-

moved the applied torque (i.e. set the controlled shear stress $\tau = 0$). We then observed the relaxation of the tool over time in terms of the shear rate $\dot{\gamma}$ at the edge of the plate, as the momentum of the sample and tool was dissipated by the effective viscosity of the fluid.

To better understand results for suspensions, we compare to a theory for a generalized Newtonian fluid, in which the function $\tau(\dot{\gamma})$ obtained from steady-state measurements is expected to be sufficient to describe the relaxation behavior in a transient flow. While general solutions for the relaxation of the tool for an arbitrary $\tau(\dot{\gamma})$ are not necessarily tractable, we can express simple equations and solutions for special cases that approximate relevant cases. Since steady-state viscosity curves for DST fluids can often be approximated by two Newtonian-like ranges with constant viscosity separated by the critical shear rate (Fig. 2), we start by writing the equations of motion for the special case of a constant viscosity, so that we can later stitch the solutions together. In a transient flow, the torque M balances the rate of change of angular momentum. In a stress-controlled flow where both the tool and the fluid remain rotating during the relaxation, this is equal to the angular acceleration $\dot{\omega}$ times the sum of the moment of inertia of the fluid I and the moment of inertia of the tool I_{tool}. Since $\dot{\omega}$ is not uniform in the fluid, we present equations for a characteristic $\dot{\omega}$ at the edge of the top plate, and the stress assuming a linear flow profile, but this makes the relationships only true as scaling relationships with an unknown proportionality constant. We will later make the relationships exact by calibrating with a Newtonian fluid. In the special case of a constant viscosity over a wide range of shear rates with a laminar flow, the torque simply relates to the viscosity by $M = \eta\omega\pi R^4/2d$ for a circular parallel plate flow geometry [24], to obtain the differential equation of motion

$$(I + I_{tool})\dot{\omega} \propto M = -\frac{\eta\pi R^4\omega}{2d} \tag{2}$$

This equation has the solution of an exponential decay for ω. Since the stress $\tau \propto M \propto \omega \propto \dot{\gamma}$ for a constant viscosity, then the solution for the stress or shear rate is also an exponential decay for a constant viscosity, given by

$$\dot{\gamma} = \dot{\gamma}(t = 0)\exp(-t/T_N)\ . \tag{3}$$

The corresponding timescale of the exponential decay T_N can be obtained from Eq. 2 to be

$$T_N = \left|\frac{\omega}{\dot{\omega}}\right| \propto \frac{2d}{\pi R^4\eta}\left(I + I_{tool}\right). \tag{4}$$

Rearranging Eq. 4 and substituting $I = \pi\rho R^4 d/2$ for the moment of inertia of the sample between circular parallel plates yields an expression for the viscosity based on the measured relaxation time

$$\eta \propto \frac{d}{T_N}\left(\rho d + \frac{2I_{tool}}{\pi R^4}\right). \tag{5}$$

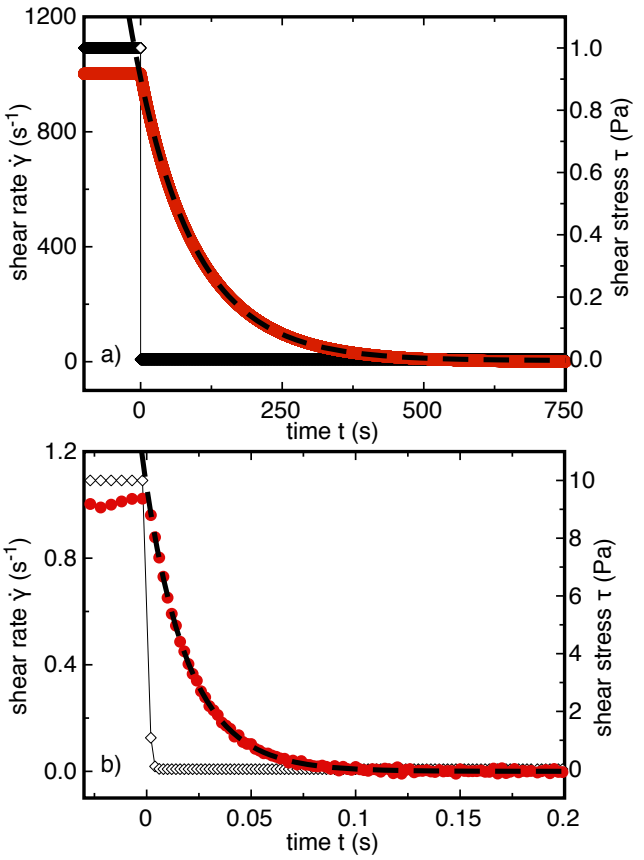


FIG. 5. (color online) The transient experiment used to measure a relaxation time T_N for a Newtonian fluid of known viscosity to calibrate Eq. 5. (a) water. (b) silicone oil. Black open diamonds: the controlled stress level τ, which was set to zero at $t = 0$ s after a steady state flow (right axis scale). Red filled circles: measured shear rate $\dot{\gamma}$ (left axis scale). Dashed line: exponential fit to obtain the relaxation timescale T_N.

To calibrate the proportionality coefficient in Eq. 5, we used water as a Newtonian fluid with known viscosity η, and measured the relaxation time T_N in a stress-controlled relaxation experiment. To ensure a laminar flow, we set a smaller gap of $d = 0.550$ mm for this experiment. We also measured a steady state viscosity curve (shown in Fig. 2 as $\phi_{wt} = 0\%$) to find the maximum shear stress where it remains proportional to shear rate before the flow becomes non-laminar due to turbulence at high Reynolds numbers. We show a linear fit to the water data for low shear rate where the flow remains laminar. Note that while the slope of the viscosity curve increases with shear rate at stresses above 1 Pa, this consequence of turbulence is not usually referred to as shear thickening. We then use this value of 1 Pa as the initial stress set point value in the stress-controlled relaxation experiments for water to maximize the stress resolution during relaxation of a laminar flow.

For the calibration experiment to measure the relaxation behavior of water, we set $\tau = 1$ Pa until the flow reached a steady shear rate $\dot{\gamma}$, then set $\tau = 0$ at a time

defined to be $t = 0$. Figure 5a shows an example of the relaxation for one of these experiments. After the steady behavior for $t < 0$, there is a gradual decay in the measured shear rate to zero. To obtain T_N, we fit the general solution to the differential equation (Eq. 3) to the data once the measured stress reached the set point value for $t > 0$. The input error on the fit was adjusted to obtain a reduced $\chi^2 \approx 1$, requiring an input error of only 0.5% of the peak shear rate. This small difference of 0.5% between the fit and the data confirms the model of Eqs. 2 and 3 describes the relaxation of Newtonian fluids well.

The calibration now allows us to determine the proportionality coefficient in Eq. 5. Using the measured relaxation time of $T_N = 105.05 \pm 0.03$ s, the measured steady-state viscosity $\eta = 9.1 \times 10^{-4}$ Pa s of the same sample of water (3% smaller than the nominal value of 9.4×10^{-4} Pa s [25]), and the measured moment of inertia of the tool $I_{tool} = 1.282 \times 10^{-5}$ kg m^2, the proportionality coefficient in Eq. 5 is calculated to be 8.1. This calibration makes the proportionality of Eq. 5 exact, which can be used to obtain a measure of viscosity η_t from transient stress-controlled relaxation flows from the relaxation time T_1 we measure for suspensions

$$\eta_t = 8.1 \frac{d}{T_1} \left(\rho d + \frac{2 I_{tool}}{\pi R^4} \right) . \qquad (6)$$

To confirm the calibration on a shorter timescale, we performed a second transient relaxation experiment for a Newtonian fluid using silicone oil (nominal viscosity of 10,000 cSt at 25°C, density $\rho = 971$ kg/m^3). We report results in Fig. 5b for the transient experiment with silicone oil with a gap $d = 1.220$ mm. We fit Eq. 5 to the data to obtain a relaxation time of $T_N = 0.0207 \pm 0.0001$ s, where the input error in the fit was adjusted to 0.5% of the peak shear rate to obtain a reduced $\chi^2 \approx 1$, just as good a fit as for the water data. We measured the steady state viscosity to be 9.9 Pa s. These values give a calibration coefficient 6% smaller than for water in Eq. 5. This difference is smaller than the 8% sample-to-sample variation in viscosity measurements due to the uncertainty in R, so remains small compared to other errors and comparisons reported in this paper. This confirms that the equipment used can reliably resolve the transient behavior for relaxation times as short as 0.21 s, shorter than all but one of the measured relaxation times reported later in this paper.

B. Relaxation in stress-controlled experiments

To test the applicability of the generalized Newtonian model and measure a relaxation time T_1 for suspensions, we initially set the shear stress τ controlled by the rheometer to a constant stress just above τ_{max} (within 10%), where τ_{max} is the maximum stress in the shear thickening range from steady state viscosity curves as shown in Fig. 2. After steady state was reached, we set the control to $\tau = 0$ at a time which was then defined to be $t = 0$. We then observed the relaxation of $\dot{\gamma}$, corresponding to the shear rate at the outer edge of the top plate, as the inertia of both the tool and the fluid was dissipated.

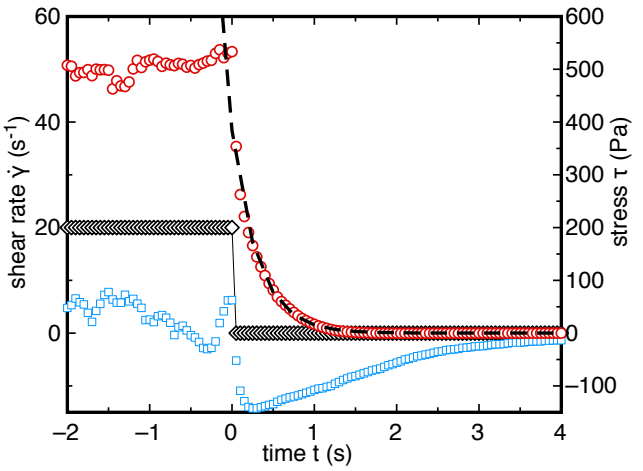


FIG. 6. (color online) An example of a transient stress-controlled experiment used to measure a relaxation time in the generalized Newtonian regime at low weight fraction ($\phi_{eff} = 57.1\%$). Black diamonds: the controlled shear stress τ (right axis scale). Red circles: measured response in shear rate $\dot{\gamma}$ (left axis scale). Blue squares: measured normal stress (right axis scale). Dashed line: exponential fit to $\dot{\gamma}$ obtain the relaxation timescale T_1. This shear rate relaxation is consistent with the generalized Newtonian model, with an initially fast relaxation due to the larger steady-state viscosity for $\dot{\gamma} \gtrsim \dot{\gamma}_c$, followed by an exponential decay for $\dot{\gamma} \lesssim \dot{\gamma}_c$ where the steady-state viscosity is nearly constant.

In Fig. 6, we show an example of a stress-controlled relaxation experiment at $\phi_{eff} = 57.1\%$, representative of the lower weight fractions we measured. While for suspensions there are fluctuations in the steady state for $t < 0$, for $t > 0$ the shear rate is again observed to decay to zero. We define the relaxation time T_1 for stress-controlled measurements by fitting this data to an exponential decay given by

$$\dot{\gamma} \propto \exp(-t/T_1) . \qquad (7)$$

Since it took a short period after $t = 0$ for the tool to reach its set point stress, we fit data once the recorded shear stress was less than 0.001 Pa, which generally happened in less than 0.02 s. The input error for the fits was adjusted until the reduced $\chi^2 \approx 1$ to obtain an error on the fit value of T_1. For the data in Fig. 6, we find that the relaxation of shear rate is consistent with an exponential within a root-mean-square difference of 0.5% of the initial stress, indicating an excellent fit of Eq. 7 in this range. The transient viscosity η_t obtained from Eq. 6 for this value of T_1 is within 43% of the value of the steady-state viscosity η_{min} at the onset of shear thickening for the same sample, comparable to the typical sample-to-sample standard deviation of 40%, consistent

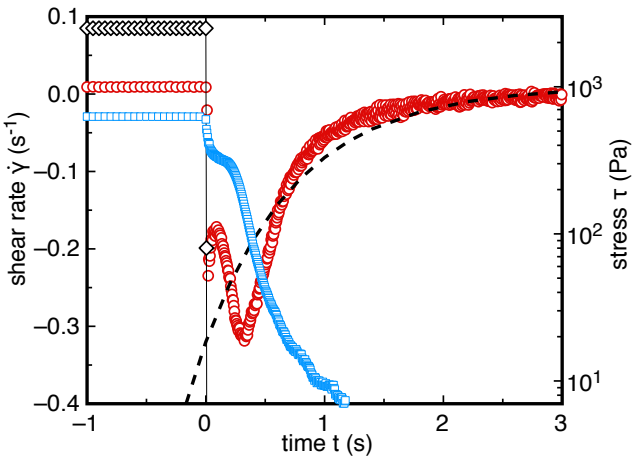


FIG. 7. (color online) An example of a transient stress-controlled experiment used to measure a relaxation time in the high weight fraction range (ϕ_{eff} = 60.3%) below ϕ_c. Black diamonds: the controlled shear stress τ (right axis scale). Red circles: measured response in shear rate $\dot{\gamma}$ (left axis scale). Blue squares: measured normal stress (right axis scale). Dashed line: exponential fit to $\dot{\gamma}$ to obtain the relaxation timescale T_1. The negative shear rate and its oscillation are inconsistent with the generalized Newtonian behavior seen in Fig. 6. Along with the positive normal stress, these features are suggestive of a temporary solid-like structure of particles in contact that can store energy elastically.

with a Newtonian fluid. However, the proportionality in the fit of Eq. 7 is significantly lower than the shear rate for $t < 0$, a difference from the Newtonian behavior in Fig. 5. Since this sample is shear thickening with 2 nearly constant viscosity regions as seen in Fig. 2, the deviation could be explained by the steady state viscosity $\eta(\dot{\gamma})$ being larger than η_{min} for $t < 0$, where $\tau > \tau_{max}$, leading to a much larger relaxation rate until the stress dropped below τ_{min} (or equivalently, the shear rate dropped below $\dot{\gamma}_c$). At later times, when $\dot{\gamma} < \dot{\gamma}_c$, the steady state $\tau(\dot{\gamma})$ curve seen in Fig. 2 is nearly linear, corresponding to a constant viscosity and an expected exponential relaxation. In Fig. 6, the proportionality fit is equal to $2.2\dot{\gamma}_c$, which is reasonably near $\dot{\gamma}_c$. These observations are consistent with a generalized Newtonian model where the steady-state viscosity curve $\tau(\dot{\gamma})$ can describe the relaxation in shear rate for this weight fraction.

We also show the normal stress measured during the relaxation experiment in Fig. 6 as blue squares using the right axis scale. The normal stress is negative for $t >$ 0, and relaxes much like the shear rate. Notably, the normal stress does not track the shear stress closely for $t > 0$, in contrast to what is typically found in DST fluids in steady-state flows [5, 20, 26]. While the generalized Newtonian model in terms of $\tau(\dot{\gamma})$ does not make explicit predictions for the normal stress, it will be insightful to compare with the normal stress at other weight fractions later.

At higher weight fraction, but still below ϕ_c, we found a different relaxation behavior. Figure 7 shows an example at ϕ_{eff} = 60.3%. In contrast to the data at lower ϕ_{eff} in Fig. 6, the shear rate became negative immediately after τ was set to zero, at a rate much larger than the initial shear rate, corresponding to the tool springing backwards. The springing backwards is suggestive of some elasticity and energy storage in the sample, such that the initial shear stored energy in strain, which could be released when the applied applied torque was removed from the tool, pushing the tool back. The single oscillation observed in Fig. 7 is another characteristic of elasticity, corresponding to an underdamped regime of an oscillator. This behavior could in principle be described by a generalized Newtonian model with linear viscoelastic term, (similar to Eq. 2, but with an additional torque $-\pi R^3 G\gamma/2$) due to the shear modulus G. We estimate $G \sim 2d(2\pi/T)^2(I + I_{tool})/\pi R^4 = 7$ Pa, where $T = 0.4$ s is the measured period of oscillation in Fig. 7. This shear modulus is small compared to τ_{max} and thus too small to be noticeable in most measurements of DST fluids. In the linear viscoelastic model, the viscous term η still relates to the timescale of an exponential decay of the oscillation with the same relationship as Eq. 5, so to obtain a relaxation timescale T_1, we fit the data for $t > 0$ to an exponential decay as in Eq. 7, despite the poor fit. Despite the ability to fit to a viscoelastic model, the negative shear rate and its oscillation differ qualitatively from the behavior at lower weight fraction shown in Fig. 6, and are likewise not predicted by the generalized Newtonian model based on the measured $\tau(\dot{\gamma})$ in Fig. 2.

The measured normal stress is also shown in Fig. 7. We only show the normal stress down to the measurement resolution, and it is smoothed over a range of 0.05 s. In this case the normal stress was positive (pushing upward on the top plate). This could be the result of a temporary system-spanning structure of solid particles in contact, which could support a load and allow elastic energy storage. Such positive normal stresses resulting from system-spanning contact networks have also been shown to be prominent in steady-state Discontinuous Shear Thickening at high weight fractions [20, 27].

C. Weight fraction regimes of different stress-controlled relaxation behaviors

To identify the range of weight fractions where the behaviors seen in Figs. 6 and 7 occur, we plot an example of the shear rate relaxation for each weight fraction we measured in Fig. 8a. The shear rate $\dot{\gamma}$ is normalized by the critical shear rate $\dot{\gamma}_c$ for each weight fraction since the initial shear rates were on very different scales due to the variation of $\dot{\gamma}_c$ with weight fraction. Due to the uncertainty of 0.3% on ϕ_{eff}, it is still difficult to make out systematic trends of relaxation times within the small regimes with a single qualitative behavior in these plots, but these plots are still helpful to identify the range of ϕ_{eff} where the different qualitative behaviors were found.

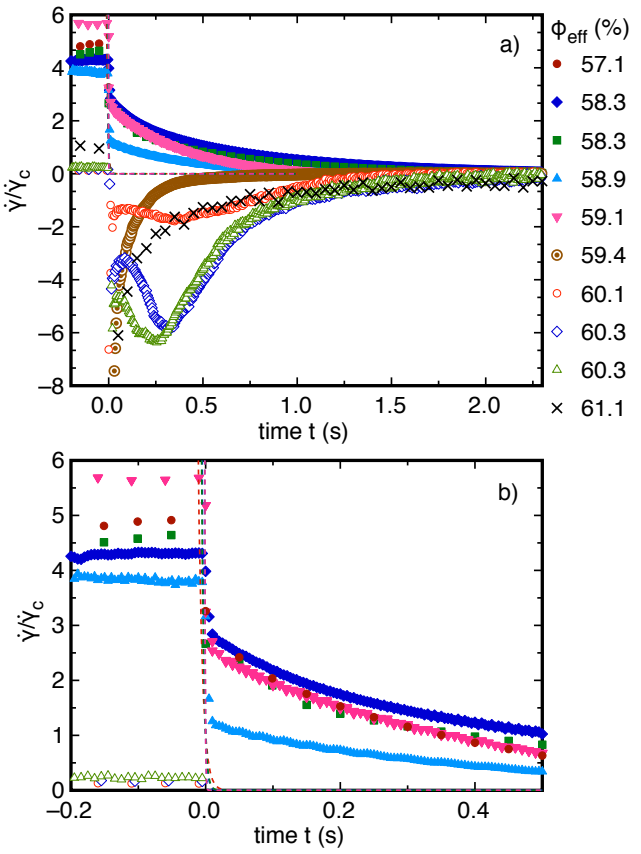


FIG. 8. (color online) Relaxation of shear rate $\dot{\gamma}$ over time t, normalized by the critical shear rate $\dot{\gamma}_c$ for different weight fractions ϕ_{eff} (listed in the legend). (a) For $\phi_{eff} > 59.4\%$, we observe negative shear rates after the stress is set to zero, and oscillation for $60.1 \leq \phi_{eff} \leq 60.3\%$ (open symbols), qualitatively inconsistent with the generalized Newtonian model. (b) Zoomed scale of panel a to see the faster initial relaxation behavior for $\phi_{eff} \leq 59.1\%$. Dashed lines: upper limit of the fast, early relaxation behavior based on the generalized Newtonian model of Eq. 6 using the maximum viscosity of the shear thickening range η_{max}, confirming the fast relaxation is consistent with the generalized Newtonian model in this range.

For samples with $\phi_{eff} \leq 59.1\%$, the relaxation behavior is qualitatively similar to the generalized Newtonian behavior shown in Fig. 6. This can be seen more clearly in Fig. 8b, where we show a zoomed in version of Fig. 8a. In this range of ϕ_{eff}, after the tool relaxation and before the exponential decay, the first value of shear rate measured after the tool relaxation (i.e. the applied shear stress is less than 0.001 Pa) is on average $(2.2 \pm 0.5)\dot{\gamma}_c$ in this range, where the uncertainty corresponds to the standard deviation of multiple experiments. We test if this faster relaxation is consistent with the generalized Newtonian model by plotting an upper limit on the shear rate $\dot{\gamma}$ as the dashed lines in Fig. 8b, based on the generalized Newtonian model of Eq. 6 using the maximum viscosity of the shear thickening range η_{max}. This is an upper limit on the initial shear rate in the generalized Newtonian model, as the actual viscosity in this range would vary between η_{max} and η_{min} as the shear rate decreases through the shear thickening range. The fact that these curves correspond to a faster relaxation than we observe (i.e. they are to the left of the data) as far as we can resolve is at least consistent with the generalized Newtonian model.

At higher weight fractions ($59.4\% \leq \phi_{eff} \leq 60.3\%$) in Fig. 8a, the shear rates are negative for $t > 0$ like in Fig. 7, inconsistent with the generalized Newtonian model of Eq. 2. The single oscillation is also seen for all of the datasets in the range $60.1\% \leq \phi_{eff} \leq 60.3\%$. At $\phi_{eff} = 59.4\%$, the oscillation was not found, which may be because the relaxation time (0.062 s) is much shorter than the oscillation period at higher effective weight fractions (0.4 s), which would typically result in the response being in the overdamped regime of a harmonic oscillator (i.e. as in a viscoelastic system).

To test which aspects of the relaxation are independent of the applied stress, we performed a series of experiments with different applied stress for $t < 0$ at a fixed ϕ_{eff} in the high-weight-fraction range. We found that the qualitative shape of the shear rate relaxation curves varies with the applied shear rate, so the curves shown in Fig. 8 should not be interpreted as the only possible qualitative results. On the other hand, some common features exist from which we can draw general conclusions. In particular, for applied stress $\tau \geq 70$ Pa up to τ_{max}, the relaxation behavior was always qualitatively inconsistent with the generalized Newtonian model, and the normal stress was always negative. For $\tau_{min} < \tau < \tau_{max}$, the measured relaxation time had no clear trend in τ, but the value varied significantly at different stresses, with a standard deviation of 0.3 decades (i.e. a factor of 2).

We also performed measurements at $\phi_{wt} = 61.1\%$, shown in Fig. 8a. Since this is above the liquid-solid transition at ϕ_c, there is no shear thickening and thus no τ_{max}, $\dot{\gamma}_c$, or values of ϕ_{eff}. Thus, we set the initial shear stress based on the value of τ_{max} from weight fractions just below ϕ_c, used the steady-state shear rate to normalize $\dot{\gamma}$, and give the raw value of ϕ_{wt} in the legend in Fig. 8a. We observe a negative stress for $t < 0$ like at the other high weight fractions, but without oscillation. Since this is above the liquid-solid transition at ϕ_c, the steady-state rheology is dominated by a yield stress. It is likely that the resulting enhanced dissipation would be enough to prevent energy storage from resulting in oscillation, analogous to overdamping a harmonic oscillator.

D. Comparison between steady state and transient viscosity as a function of weight fraction

We next quantitatively test how well the generalized Newtonian model describes the relaxation time T_1, to determine whether the failure of Eq. 7 to describe the shape of the transient relaxation curves is merely due

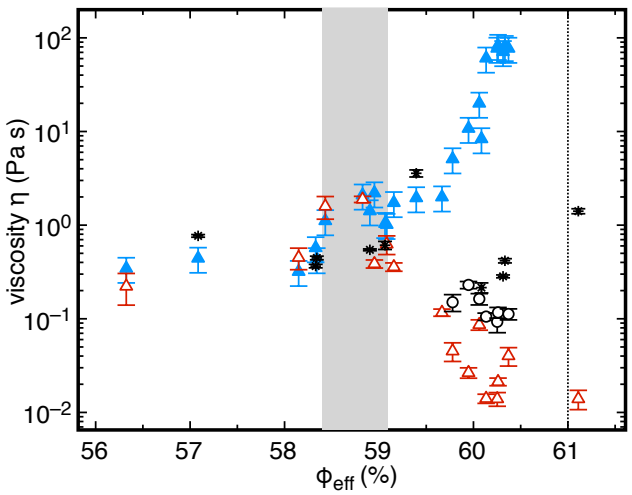


FIG. 9. (color online) Steady state and transient viscosities as a function of effective weight fraction ϕ_{eff}. Blue solid triangles: steady state viscosity η_{min}. Black stars: transient viscosity η_t for shear-stress-controlled relaxation experiments. Red open triangles: transient viscosity η_t for shear-rate-controlled experiments based on relaxation time T_1. Black open circles: transient viscosity η_t for shear-rate-controlled experiments based on the relaxation time T_2. Vertical dotted line: liquid-solid transition at $\phi_{eff} = \phi_c$. The transient viscosity in both control schemes deviates from the steady state viscosity at large ϕ_{eff}, by up to 4 orders of magnitude. Vertical gray band: uncertainty in the transition delineating whether relaxation behavior follows the generalized Newtonian model.

to a missing non-viscous term in the equation of motion such as an elastic term, or also involves a failure to correctly describe the energy dissipation via the relationship between T_1 and η_t in Eq. 5. We do this by comparing the transient viscosity η_t with the steady state viscosity η_{min} as a function of effective weight fraction ϕ_{eff} in Fig. 9.

In Fig. 9, the solid triangles show η_{min} as a best estimate of the hydrodynamic viscosity obtained as in Fig. 1. The error bars represent the standard deviation of the mean of the four ramps. The steady state viscosity increases with ϕ_{eff}, with a typical apparent divergence as $\phi_{eff} \to \phi_c$ [8, 9].

The stars in Fig. 9 represent the transient viscosity η_t from the stress-controlled relaxation measurements, calculated from Eq. 6 where T_1 is obtained from the fit of Eq. 7. The errors shown are propagated from the standard deviation of the mean of T_1 for 5 repeated measurements of each sample, added in quadrature with the fit errors.

For our lowest weight fractions $\phi_{eff} \leq 59.1\%$, where the relaxation behavior seen in Fig. 8 was qualitatively consistent with the generalized Newtonian model, we find that the transient viscosity η_t is scattered around the steady state viscosity η_{min}. The root-mean-square difference between η_t and η_{min} is 47%. This is larger than the average errors on η_t or η_{min} for individual samples of 5% for stress-controlled data and 15% for rate-controlled data. However, the 47% difference is comparable to the sample-to-sample variation in η_{min} of 40%, measured as the root-mean-square difference between the measured η_{min} and a best power law fit of η_{min} in the same range of ϕ_{eff}. This agreement within the scatter confirms that the relaxation behavior is consistent with that of a generalized Newtonian fluid in this range of ϕ_{eff}, where the exponential relaxation rate relates to η_{min}.

At the next lowest weight fraction, $\phi_{eff} = 59.4\%$, corresponding to the high-weight-fraction range of Fig. 8, η_t is 83% larger than η_{min}, within 2 standard deviations of the scatter of η_{min}. However, the relaxation behavior was qualitatively inconsistent with that of a generalized Newtonian fluid, since the shear stress dropped negative for $t > 0$, with the opposite sign of a Newtonian fluid. Thus, this weight fraction remains the lowest at which we find the relaxation behavior to be inconsistent with the prediction for a generalized Newtonian fluid based on the viscosity curves in Fig. 2

At higher weight fractions, $60.1\% \leq \phi_{eff} < 61.0\%$, where the qualitative behavior shown in Fig. 8 is also inconsistent with the generalized Newtonian model, we find that the transient viscosity η_t is smaller than the steady state viscosity η_{min} by 1.5 to 2.5 orders of magnitude in Fig. 9. We note that accounting for the non-Newtonian viscosity function $\tau(\dot{\gamma})$ cannot reduce this discrepancy; since η_{min} is the minimum viscosity in the viscosity curve, the values shown for the steady-state viscosity are the lowest we could have chosen at any given weight fraction, and so the discrepancy would be even larger if we compared to viscosity values of different shear rates or tried to account for the non-Newtonian shape of $\tau(\dot{\gamma})$.

For $\phi_{wt} > \phi_c$, we could still measure a relaxation time despite the fact that the material was a solid in the sense that it had a yield stress. We found a transient viscosity in between the steady state viscosity and transient viscosity at ϕ_{eff} just below ϕ_c. Based on the steady-state $\tau(\dot{\gamma})$ curve, no flow is expected for $\tau < \tau_{min}$. If we include strain-dependent rheology as in the viscoelastic model, yield stress materials generally have a stress-strain curve that goes to zero strain in the limit of zero stress. This would lead to an expectation of the tool springing back with a negative shear rate to relax the strained state, as observed in Fig. 8. However, the steady-state curves for yield stress fluids have an infinite viscosity in the limit of zero shear rate, and even at the initial shear rate used, an effective viscosity close to η_{max} of the highest $\phi_{eff} < \phi_c$. That puts a lower bound on the effective viscosity for the generalized Newtonian model on the order of 10^5 Pa s. The fact that η_t is on the order of 1 Pa s for $\phi_{wt} > \phi_c$, and much lower than the values of η_{min} for $\phi_{eff} < \phi_c$, is inconsistent with the generalized Newtonian model.

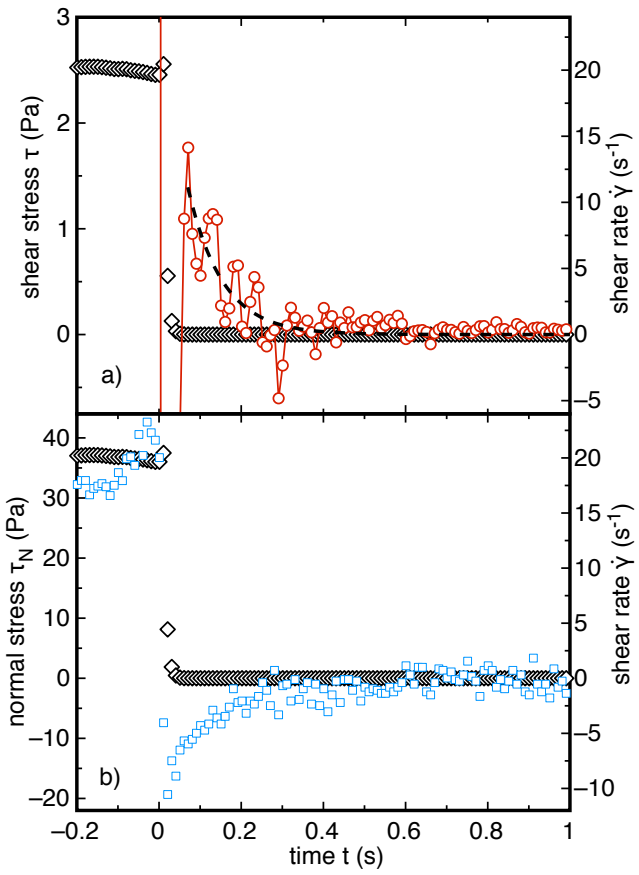


FIG. 10. (color online) (a) An example of a transient rate-controlled experiment in the generalized Newtonian regime at low weight fraction ($\phi_{eff} = 58.1\%$). Black diamonds: the controlled shear rate $\dot{\gamma}$ (right axis scale), which was set to zero for $t > 0$ after a steady flow. Red circles: measured response in shear stress τ (left axis scale). Dashed line: exponential fit to τ to obtain the relaxation timescale T_1. (b) Blue squares: measured normal stress (right axis scale). This relaxation behavior is qualitatively consistent with the generalized Newtonian model.

E. Relaxation in rate-controlled experiments

To test the generality of the observed relaxation behaviors for different types of flows with different boundary conditions, we also performed relaxation measurements in rate-controlled flows. These experiments were analogous to the stress-controlled experiments with the roles of shear stress and shear rate swapped. In these measurements, we first rotated the tool at a shear rate $\dot{\gamma}$ about 60% higher than the critical shear rate $\dot{\gamma}_c$ to achieve a steady-state in the stress at a value above the maximum stress τ_{max} of the shear thickening range (i.e. in the high stress regime seen in Fig. 1). After a steady-state was reached, we attempted to stop the tool by setting the shear rate to $\dot{\gamma} = 0$, and measured the relaxation of the stresses on the tool over time due to the relaxation of the fluid.

Figure 10a shows an example of both the controlled shear rate $\dot{\gamma}$ and the response in shear stress τ as a function of time, for a sample at low $\phi_{eff} = 58.1$ % ($\dot{\gamma}_c^{-1} = 0.24$ s). After the initial steady behavior for $t < 0$ (initially at ≈ 100 Pa), there was a transient of the tool around $t = 0$ before the shear rate settled down to the set point for $t > 0$. We note that the rheometer responds more slowly in rate-control than stress control, so the transient time for the shear rate to change from its initial setpoint value to zero is typically much longer than for the stress in Figs. 5, 6, and 7. Data in this range is significantly affected by the PID control loop that controls the rotation of the tool, and should not be considered part of the sample response.

After this transient of the tool, we observe a large negative stress (peak recorded magnitude of -260 Pa) in Fig. 10a. This negative stress is to be expected in a rate-controlled flow even for a Newtonian fluid: after the plate stops but the suspension continues to flow, it applies a drag force on the top plate pushing it in its initial direction of motion, but with a force in the opposite direction as when the plate was driving the flow.

As the top plate decelerates in rate-controlled experiments, the mean flow profile for a Newtonian fluid would have to transition from a plane Couette flow in the steady state for $t < 0$ to a more parabolic profile that satisfies the no-slip condition at the top plate after it stopped moving. This is in contrast to stress control experiments where the mean flow profile for a Newtonian fluid could remain that of a plane Couette flow during the entire experiment. This change in profile requires a rapid energy dissipation as the shear rate near the top plate becomes very large during the transient compared to the steady-state profile, and a corresponding large torque on the tool during the transient. Once the shear profile evolves from its initial plane Couette profile to a more parabolic profile, the drag force on the plate is expected again to oppose the initial direction of flow, resulting in a positive stress. After this transient with the negative stress, we observed a decay in stress from a positive value. We find the stress at the start of this slower decay is $1.5\tau_{min}$, analogous to the stress-controlled experiments in Fig. 6. It appears that the faster relaxation at higher effective viscosity in the shear thickening regime occurred over about the same time interval as the flow-profile evolution. Despite the unusual transient behavior immediately after $t = 0$, the relaxation behavior at this weight fraction appears to be consistent with the generalized Newtonian model.

In rate-controlled experiments, once the transient of the tool and the shear profile evolution are done, the expected solution for the shear stress decay for a constant viscosity, i.e. where $\tau \propto \dot{\gamma}$, is the same as Eq. 7 with a swap of τ for $\dot{\gamma}$. To obtain a relaxation timescale T_1 for rate-controlled experiments, we fit the measured $\tau(t)$ during the relaxation to the exponentially decaying function

$$\tau \propto \exp(-t/T_1) + constant\ . \qquad (8)$$

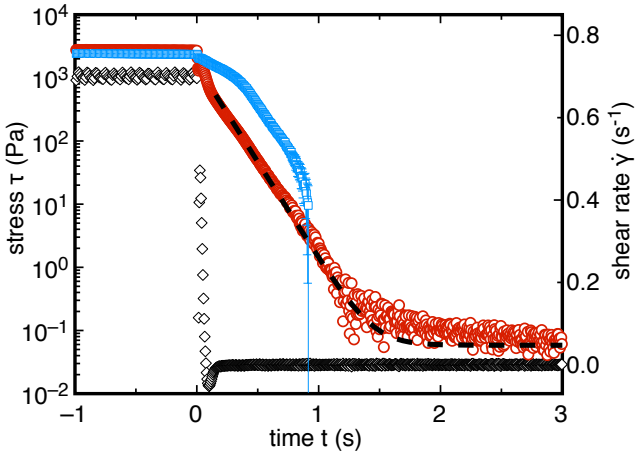


FIG. 11. (color online) An example of a transient rate-controlled experiment on the low side of the high-weight-fraction range (ϕ_{eff} = 59.7%). Black diamonds: the controlled shear rate $\dot{\gamma}$ (right axis scale). Red circles: measured shear stress τ response (left axis scale). Blue squares: measured normal stress τ_N. Dashed line: exponential fit to τ to obtain the relaxation timescale T_1. The lack of a quick drop in shear stress to negative values or near τ_{min} just after $t = 0$ is inconsistent with the generalized Newtonian model.

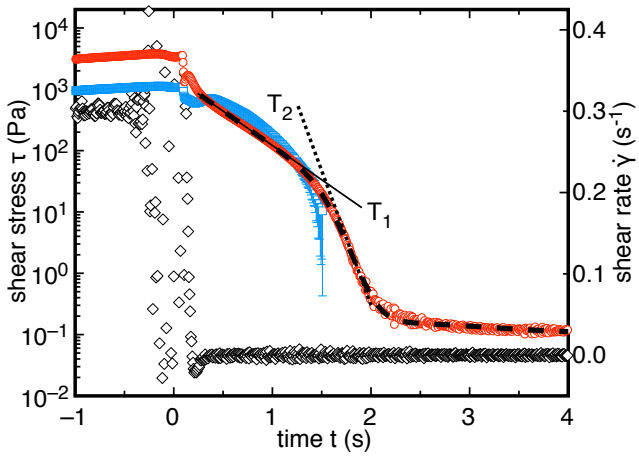


FIG. 12. (color online) An example of a transient rate-controlled experiment on the high side of the high-weight-fraction range (ϕ_{eff} = 60.1 %), where two exponential scaling regimes are found. Black open diamonds: the controlled shear rate $\dot{\gamma}$ (right axis scale). Red open circles: measured shear stress τ response (left axis scale). Dashed line: exponential fit of Eq. 9 to obtain the relaxation timescales T_1 (dotted line) and T_2 (solid line). Blue squares: measured normal stress τ_N. The lack of a quick drop in shear stress to negative values or near τ_{min} just after $t = 0$ is inconsistent with the generalized Newtonian model.

The addition of the constant accounts for the yield stress found at higher weight fractions. An example fit is shown in Fig. 10a. To avoid a contribution from the transient of the tool immediately after the shear rate was set to zero, we generally started fitting after $\dot{\gamma}$ was less than 5% of its initial $t < 0$ set point value, and in cases like in Fig. 10 where the sign of the shear stress first went negative after $t = 0$, we fit only after the stress was positive again. The input error on fits was adjusted until the reduced $\chi^2 \approx 1$ to obtain an error on the fit value of T_1, as in the fits of Eq. 7. The data in Fig. 10 were fit with no constant term, resulting in a good fit of the predicted exponential relaxation, which is qualitatively consistent with the generalize Newtonian model, even though there is a large scatter in which the root-mean-square difference between the data and the fit over the first 0.6 s of the relaxation is 17% of the proportionality coefficient.

The measured normal stress for the rate-controlled relaxation experiment at ϕ_{eff} = 58.1% is shown in Fig. 10b. In this case the normal stress was negative for $t > 0$, and relaxed along with the shear stress, analogous to what was found in stress-controlled measurements in the same weight fraction range in Fig. 6.

Figure 11 shows an example of the stress relaxation for a sample on the low side of the high-weight-fraction range, ϕ_{eff} = 59.7 % ($\dot{\gamma}_c^{-1}$ = 2.4 s). The lack of an immediate drop to a negative shear stress or to near τ_{min} after $t = 0$ is qualitatively different from the stress-controlled relaxation observed in the same weight fraction range in Fig. 7. Despite this observation – which is qualitatively inconsistent with the generalized Newtonian model – the exponential fit of Eq. 8 to obtain T_1 is very good, with a root-mean-square difference of 2.4% of the initial stress, indicating that we can still obtain a clear good measure of energy dissipation.

The measured normal stress is also shown in Fig. 11. We only show the normal stress down to the measurement resolution (∼ 10 Pa), and plot this systematic error as the error bar in the figure. In this case the normal stress was positive, similar to that found in stress-controlled measurements in the same weight fraction range in Fig. 7. It tends to follow a similar trend as the shear stress, however, it is not proportional to the shear stress over a wide range of stress as is typical of steady-state DST [20, 26].

At the highest weight fractions below ϕ_c, the stress relaxation appears to have two exponential regimes, as shown for example in Fig. 12 at ϕ_{eff} = 60.1 % ($\dot{\gamma}_c^{-1}$ = 9.1 s). Other than the two exponential scaling regimes, the relaxation behavior is qualitatively similar to Fig. 11. While the lack of a quick relaxation to τ_{min} or negative stress is inconsistent with the generalized Newtonian model, the two exponential ranges could in principle correspond to constant viscosity regions of a steady-state viscosity curve. To test this, we obtain relaxation times T_1 and T_2 for each regime, using the fit function

$$\tau \propto \left(\frac{1}{\exp(-t/T_1)} + \frac{1}{\exp(-t/T_2)} \right)^{-1} + constant \ . \quad (9)$$

We fit this to the data in Fig. 12 in two steps to provide better fit stability. The first step fits Eq. 8 to the data the same way as in Fig. 11 to fit the earlier, slower relaxation. After T_1 is determined from this fit, we fit Eq. 9 to the

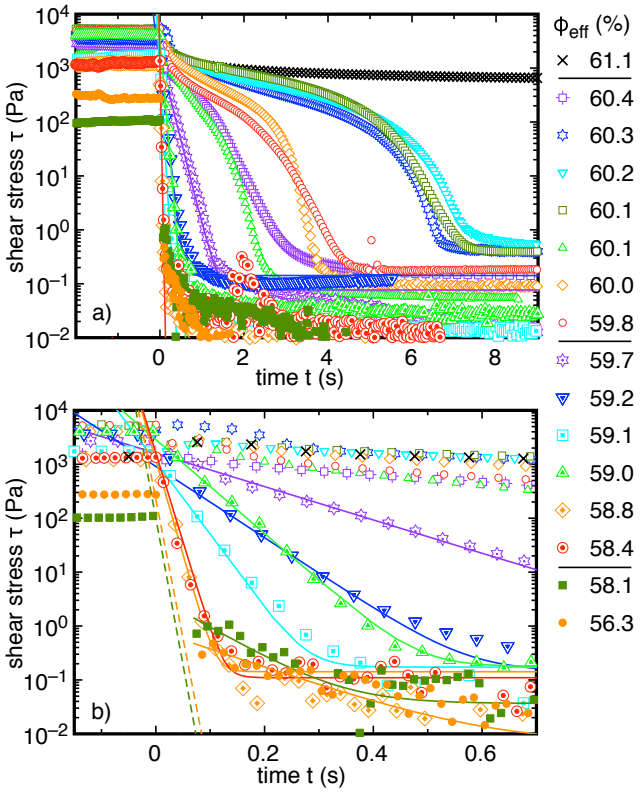


FIG. 13. (color online) Relaxation of shear stress τ over time t for different weight fractions ϕ_{eff} listed in the legend. For ease of comparison, the symbols are the same as used in Fig. 2, and different filling types correspond to different qualitative behaviors. (a) Dual-exponential relaxation is found for $59.8\% \leq \phi_{eff} < 61.0\%$ (open symbols), while single exponential relaxation is found for $58.4\% \leq \phi_{eff} \leq 59.7\%$ (partially filled symbols). (b) Zoomed scale of panel a to show that for $\phi_{eff} \leq 58.1\%$ (closed symbolss), there is a faster initial relaxation followed by an exponential decay. Solid lines: fits of Eq. 8 to the samples with single exponential behavior. Dashed lines: upper limit of the fast, early relaxation behavior for $\phi_{eff} \leq 58.1\%$ based on the generalized Newtonian model of Eq. 4 using the maximum viscosity of the shear thickening range η_{max}, confirming the fast relaxation is consistent with the generalized Newtonian model.

data with only T_2 as a free parameter, and only to the range $\tau \leq 10$ Pa, with the same error fitting technique.

The measured normal stress is also shown in Fig. 12. Again, we only show the normal stress down to the measurement resolution, and plot this systematic error in the figure. In this case the normal stress was again positive and followed a similar trend as the shear stress, qualitatively similar to that found in in Fig. 11.

F. Weight fraction regimes of different rate-controlled relaxation behaviors

To determine the range of weight fraction ranges of the different relaxation behaviors seen in Figs. 10-12, we show in Fig. 13a examples of the stress relaxation $\tau(t)$ for rate-controlled data at all weight fractions measured. We will use this to compare to the stress-controlled data in later sections.

The dual-exponential relaxation behavior shown for example in Fig. 12 is found throughout the range $59.8\% \leq \phi_{eff} < \phi_c$ ($\dot{\gamma}_c^{-1} \geq 3.4$ s, open symbols in Fig. 13). Many of these higher weight fraction samples relax to a non-zero stress value in the limit of large time, consistent with the yield stress measured from the steady-state measurements in Fig. 2. The transition between the two exponential scaling regimes was consistently found to be on the scale of $\tau \sim 10^2$ Pa. For comparison, in stress-controlled experiments the stress dropped almost instantaneously from the initial steady-state value to 0, so there was no measurable time period over which two different exponential relaxation regimes in stress could be observed in stress-controlled experiments if the stress range is what determines the relaxation rate. Thus, the observation of two exponential relaxation regimes is not inconsistent with the stress-controlled measurements in Fig. 8.

The single-exponential relaxation behavior shown for example in Fig. 11 is found in the range $58.4\% \leq \phi_{eff} \leq 59.7\%$ (0.33 s $\leq \dot{\gamma}_c^{-1} \leq 2.7$ s, partially filled open symbols in Fig. 13). These relax much faster than at higher ϕ_{eff}. None of the data for $\phi_{eff} \geq 58.4\%$ ($\dot{\gamma}_c^{-1} \geq 0.33$ s) show the initial drop to a negative stress or to near τ_{min} expected from the generalized Newtonian model.

To see the behavior at low weight fractions $\phi \leq 58.1\%$ ($\dot{\gamma}_c^{-1} \leq 0.24$ s, solid symbols) in Fig. 13, we show a zoomed in version of panel a in panel b. To better see the signal in the noisy background, the data shown here are smoothed over a range of 0.025 s for $\phi_{eff} \leq 58.8\%$ and a range of 0.050 s for other data sets after the shear rate is set to zero. For $\phi \leq 58.1\%$, extrapolations of the exponential fits of Eq. 8 to the raw data fall well below the stress at $t < 0$, but are on average $(1.6 \pm 0.9)\tau_{min}$, analogous to the stress-controlled experiments in the low-weight-fraction range shown in Fig. 8, suggesting the initial fast relaxation is again due to the higher viscosity for $\tau > \tau_{min}$.

We note that we performed rate-controlled relaxation experiments at 5 different weight fractions in the range $56.0\% < \phi_{eff} \leq 58.1\%$, but in 3 of those cases we could not resolve any stress for $t > 0$ as the stress was comparable to the noise level. We do not present data for those cases here, or include it in later comparisons of T_1.

For $\phi_{wt} = 61.1\% > \phi_c$, the suspension behaves as a yield stress fluid as seen in Fig. 2, so there is no ϕ_{eff} scale and the raw value of ϕ_{wt} is given in Fig. 13 instead. There is also no τ_{max}, so in this case we instead set the initial shear rate based on the value of τ_{max} for ϕ_{eff} just

below ϕ_c.

G. Calibration of transient viscosity for rate-controlled data

Equation 6 which relates the relaxation time to transient viscosity is only valid for experiments performed under stress control, as it assumes the tool continued to rotate after we set $\tau = 0$. In shear-rate-controlled experiments, the tool was no longer rotating significantly at the relaxation set point $\dot{\gamma} = 0$. Therefore, the inertia of the tool no longer contributed to the angular momentum of the system, so I_{tool} should be removed from Eq. 5 when applied to rate-controlled flows. Furthermore, since the flow profile for a Newtonian fluid would transition from a plane Couette flow in the steady state for $t < 0$ to a more parabolic profile after the top plate stopped moving to satisfy the no-slip boundary condition at the top plate in rate-controlled experiments, the different flow profile would result in a different proportionality coefficient for rate-controlled experiments than for stress-controlled experiments as given in Eq. 6. Therefore, for rate-controlled experiments, we reduce the model from Eq. 6 to

$$\eta_t \propto \frac{\rho d^2}{T_1} \ . \tag{10}$$

We attempted a calibration under rate-control with water. Initially we observed a large negative stress, similar to the example in the generalized Newtonian regime in Fig. 10. For $t > 0$, large fluctuations in the measured stress drowned out any relaxation signal we attempted to measure. Even without the contribution of I_{tool} to the total inertia of the system, the relaxation time would be expected to be resolvable based on Eq. 10. On the other hand, this lack of measured stress is consistent with the data for $\phi_{eff} \leq 58.1\%$ in Fig. 13 where the stress dropped by 1-3 orders of magnitude during the tool deceleration and evolution of the shear profile, which would put the stress below our measurement resolution for water. While we were unable to calibrate the rate-controlled experiments directly with this technique, this observation confirms that the data for $\phi_{eff} \leq 58.1\%$ in Fig. 13 are consistent with the expectations of a generalized Newtonian fluid.

Instead, we calibrate the relaxation times from rate-controlled experiments by fitting to results from stress-controlled data. The prediction of the relaxation time from the generalized Newtonian model (Eq. 6) agrees with the stress-controlled relaxation data at low weight fractions $\phi_{eff} \leq 59.1\%$, seen quantitatively in Fig. 9, as well as qualitatively, as seen in Fig. 8. Likewise, the rate-controlled data for $\phi_{eff} \leq 58.1\%$ were qualitatively consistent with the generalized Newtonian model. Thus, we can reasonably assume that the flow in rate-control in this weight fraction range is also quantitatively consistent with the generalized Newtonian model, obtain the scaling coefficient for Eq. 10, and check for self-consistency later. We obtain the scaling coefficient by taking the ratio of the transient viscosity obtained from rate-controlled experiments to the steady-state viscosity from Eq. 10 assuming a scaling coefficient of 1, and average over the 2 values of $\phi_{eff} \leq 58.1\%$. The scaling factor obtained is 15 ± 7. Hence, we can re-write Eq. 10 with a scaling factor as

$$\eta_t = 15\frac{\rho d^2}{T_1}. \tag{11}$$

The resulting values of the transient viscosity η_t for both T_1 and T_2 are shown in Fig. 9. The values of η_t from rate-controlled data using this scaling are consistent with the steady-state η_{min} within their errors of 30% for the same samples for $\phi_{eff} \leq 58.8\%$. These η_t values are consistent with the generalized Newtonian model over this wider range than the fit.

As another self-consistency check for the calibration of Eq. 11, we use it to estimate the timescale of the initial fast relaxation for the data for $\phi \leq 58.1\%$ shown in Fig. 13b. We plot the shear stress as the dashed lines in Fig. 13b for the predicted exponential decay of the generalized Newtonian model from Eq. 8 using the maximum viscosity of the shear thickening range η_{max} as an estimate of the transient viscosity, since the effective viscosity is close to η_{max} in the steady-state for the initial shear rates just above $\dot{\gamma}_c$. This is a rough estimate because the shear profile must change in rate-controlled relaxation experiments during this fast decay, which could change the dissipation rate relative to that of the steady-state shear profile. The fact that this prediction is about a factor of 2 faster than the measured relaxation to near τ_{min}, where the exponential decay starts is again plausibly consistent with the generalized Newtonian model, as far as we can resolve in this weight fraction range.

The transient viscosities η_t do start deviating significantly from the steady state η_{min} for $\phi_{eff} \geq 59.0\%$ ($\dot{\gamma}_c^{-1} \geq 0.60$ s), in the middle of the range where the single-exponential relaxation behavior shown for example in Fig. 11 was found. This deviation reaches up to 4 orders of magnitude at the largest $\phi_{eff} < \phi_c$ that we measured. In this range, the values of η_t based on rate-controlled measurements disagree with those based on stress-controlled measurements, by about a factor of 3 for T_2 and an order of magnitude for T_1. This disagreement in values of η_t for different flows indicates that η_t is not an intrinsic property in this high ϕ_{eff} range.

H. Comparison of time scales

So far we have represented the relaxation behavior in terms of the transient viscosity η_t, but we can make some different scaling comparisons, and determine whether the viscosity or relaxation time is more intrinsic, if we also plot the relaxation behavior in terms of timescales. We show both relaxation times and the viscous dissipation timescale corresponding to the steady-state viscosity as

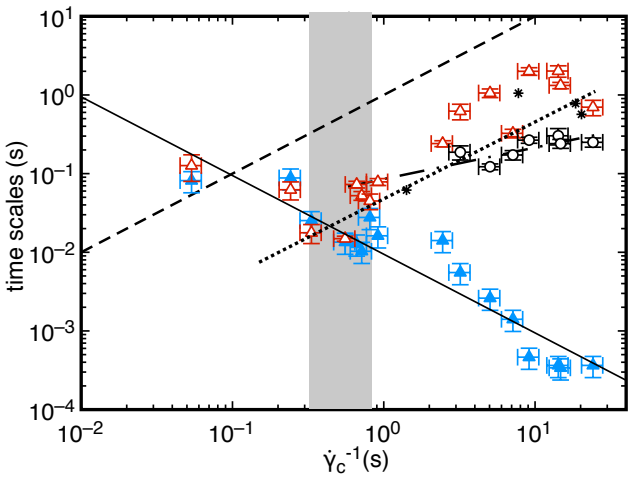


FIG. 14. (color online) Relaxation times as a function of inverse critical shear rate $\dot{\gamma}_c^{-1}$, which is a proxy for the weight fraction. Red open triangles: T_1 for rate-controlled data. Black open circles: T_2 for rate-controlled data. Blue solid triangles: generalized Newtonian model prediction T_N. Solid line: power law fit of T_N. Dotted line: power law fit to T_1 in the range it deviates from the generalized Newtonian model. Dashed-dotted line: power law fit to T_2. Dashed line: the timescale corresponding to the inverse critical shear rate $\dot{\gamma}_c^{-1}$, which has a similar scaling as T_1 at large weight fraction. Black stars: T_1 for stress-controlled data, which agree with T_1 for rate-controlled data in the high-weight fraction range where the generalized Newtonian model fails (right side of the gray band), indicating the relaxation time is a more universal quantity than viscosity in this range.

a function of the time scale equal to the inverse critical shear rate $\dot{\gamma}_c^{-1}$ in Fig. 14. $\dot{\gamma}_c^{-1}$ is also a proxy for the weight fraction, where ϕ_{eff} increases with $\dot{\gamma}_c^{-1}$, but with much higher resolution near the critical point since it diverges as ϕ_{eff} approaches ϕ_c. Rate-controlled data are replotted from Fig. 9 to Fig. 14. A viscous dissipation timescale T_N for the steady-state flow is obtained from the steady-state viscosity η_{min} based on Eq. 11 by replacing η_t with η_{min}. A power law fit to the corresponding timescale yields an exponent -0.92 ± 0.05, consistent within 2 standard deviations of the known inverse scaling between onset viscosity $\eta_{min}(\propto T_N^{-1})$ and onset shear rate $\dot{\gamma}_c$ [8, 23]. The same general trends can be seen as in Fig. 9, for example the transient time scale T_1 grows as $\dot{\gamma}_c^{-1}$ increases (i.e. as weight fraction increases) for 58.4% $\leq \phi_{eff} \leq \phi_c$ ($\dot{\gamma}_c^{-1} \geq 0.33$ s), while the viscous dissipation timescale T_N based on the steady-state flow decreases.

The viscous dissipation timescale predicted from the generalized Newtonian model is a quantity that depends on the dimensions and boundary conditions of the system, and is not an intrinsic material property like the viscosity of a Newtonian fluid. Equation 4 predicts the viscous dissipation timescale T_N coming from the stress-controlled relaxation would be larger than from the rate-controlled relaxation by a factor of $(I_{tool} + I)/I = 15$. To test this, we plot the relaxation time T_1 from stress-controlled data as stars in Fig. 14, only plotting data in the range where the generalized Newtonian model fails for the stress-controlled data (59.4% $\leq \phi_{eff} < \phi_c$, $\dot{\gamma}_c^{-1} \geq 1.4$ s). We find that the stress-controlled relaxation times collapse with the rate-controlled T_1 in this range. This suggests that the relaxation time T_1 is a more universal quantity (i.e. for different types of flow control) than the viscosity in this high weight fraction range, at least for a given system size. Physically, it indicates that the relaxation time is not determined by the time it takes to dissipate the angular momentum of the system in this high weight fraction range according to the generalized Newtonian model, which is larger in stress-controlled experiments due to the addition of the tool inertia, but could instead be a relaxation time of an internal structural of the suspension.

To gain some insight into the scaling of the relaxation time in the high weight fraction range, we least-squares fit a power law fit to $T_1(\dot{\gamma}_c^{-1})$ in the range where it deviates from the generalized Newtonian model in Fig. 14. We obtain a slope 1.0 ± 0.1. We adjusted the input errors to the fit until the reduced $\chi^2 \approx 1$ so that the error represents an uncertainty on the slope assuming a power law fits the data. An extrapolation of T_1 based on the power law fit of this range diverges to infinity in the limit of $\dot{\gamma}_c^{-1} \to \infty$ (dotted line), corresponding to the liquid-solid transition as $\phi \to \phi_c$ [8]. A similar power law fit to T_2 in this range yields an estimate for a slope of 0.4 ± 0.2 (long dashed line). For comparison with T_1, we plot the timescale $\dot{\gamma}_c^{-1}$ in Fig. 14. While this does not match any of the other time scales plotted, the power law exponent is consistent with that of T_1 of 1.0 ± 0.1 at large $\dot{\gamma}^{-1}$. It is possible that in the limit of large weight fraction, T_1 may be determined by $\dot{\gamma}_c$. It was proposed in some early shear thickening models based on hydrodynamic mechanisms that $\dot{\gamma}_c^{-1}$ is proportional to a contact relaxation time – a timescale it takes for particles in contact or near-contact to move significantly away from each other when they are pushed by the same repulsive forces that determine the onset of shear thickening, and resisted by viscous drag [28]. The agreement with the scaling argument suggests that the unusually long relaxation times we observe at high weight fractions may be due to this contact relaxation time.

VI. DISCUSSION

A. Range of generalized Newtonian behavior

In both rate- and stress-controlled relaxation experiments, we found suspensions to relax as a generalized Newtonian fluid where the relaxation behavior can be described by the steady-state relation $\tau(\dot{\gamma})$ at low weight fractions; specifically $\phi_{eff} \leq 59.1\%$ for stress-controlled data, and $\phi_{eff} \leq 58.1\%$ in rate-controlled data. We found the relaxation behavior to be qualitatively incon-

sistent with the generalized Newtonian model for $\phi_{eff} \geq 59.4\%$ for stress-controlled data, and $\phi_{eff} \geq 58.4\%$ for rate-controlled data. Given the uncertainty of 0.3% on of ϕ_{eff}, we calculate a best estimate of the transition as a mean of the four weight fractions as $\phi_{eff} = 58.8\% \pm 0.3\%$ ($\dot{\gamma}_c^{-1} = 0.54$ s. This is consistent within about 1 standard deviation of the transitions measured separately from rate- or stress-controlled data. This range is shown as the gray band in Figs. 9 and 14. This gray band is also consistent with the intersection of the fits of T_1 and T_N in Fig. 14 where the timescales start deviating from each other. We henceforth refer to the weight fraction where the generalized Newtonian model starts to fail as $\phi_{eff} = 58.8\% \pm 0.3\%$ when not referring to specific stress- or rate-controlled experiments.

In the high-weight-fraction range ($58.8\% < \phi_{eff} < \phi_c$, $\dot{\gamma}_c^{-1} > 0.54$ s) where the relaxation behavior was inconsistent with the generalized Newtonian model, we found consistently discontinuous steady-state viscosity curves for the same samples shown in Fig. 2. At lower weight fractions, whether or not the viscosity curves were discontinuous was less consistent on repetition, resulting in average curves that are steep, but not discontinuous. From this correspondence we can conclude that the relaxation behavior is inconsistent with the generalized Newtonian model specifically at weight fractions where the viscosity curve is consistently discontinuous in rate-controlled experiments.

B. Normal stress and system-spanning structures

In the generalized Newtonian regime in the low weight fraction range ($\phi_{eff} < 58.8 \pm 0.3\%$, $\dot{\gamma}_c^{-1} < 0.54$ s), we always observed negative normal stress during the relaxation. In contrast, for $\phi_{eff} > 58.8 \pm 0.3\%$ where we found disagreement with the generalized Newtonian model, we always observed positive normal stress during the relaxation. This correspondence indicates the sign of the normal stress is also a good indicator of whether or not the relaxation follows generalized Newtonian behavior.

In the high-weight-fraction regime ($58.8\% < \phi_{eff} < \phi_c$, $\dot{\gamma}_c^{-1} > 0.54$ s), we observed a negative shear rate and oscillation during relaxation in stress control (e.g. Fig. 7). The positive normal stress observed during relaxation could be the result of system-spanning structures of particles pushing against each other. The positive normal stress in steady state DST is often taken as indication of a system-spanning network of particles in compression which push against each other and the rheometer plates [20, 27, 29], and these networks are argued to play an important role in supporting frictional interparticle contacts which transmit both normal and shear stresses [20, 27]. The plateau in stress at $\tau \approx \tau_{max}$ for higher shear rates in Fig. 2 for this weight fraction range is consistent with the model of frustrated dilation [20], where these normal and shear stresses are limited by surface tension at the boundary, mostly independent of shear rate. Thus, the interpretation of system-spanning structures of particles in contact at high weight fractions is consistent with steady-state interpretations.

In contrast, the negative normal stress observed during relaxation in the generalized Newtonian regime ($\phi_{eff} < 58.8\%$, $\dot{\gamma}_c^{-1} < 0.54$ s) likely originates from hydrodynamic effects. This is also the same weight fraction range where we observed a linear relation in the steady-state $\tau(\dot{\gamma})$ curve for $\tau > \tau_{max}$ (Fig. 2) for the same samples, instead of the plateau at $\tau \approx 10^3$ Pa seen at higher ϕ_{eff}. This feature is suggestive of a viscous hydrodynamic scaling at the low weight fractions, which might be expected from the hydrocluster model [10], or a model in which shear thickening is a transition between two viscous scaling regimes with different structure [30].

Perhaps surprisingly, the normal stress was still positive in the steady-state before the transition to negative normal stress during relaxation in the generalized Newtonian regime. The negative normal stress during relaxation indicates that, if there was a system-spanning contact network in the steady-state, its relaxation must have been fast compared to the viscous dissipation time T_N in this weight fraction range. The structural relaxation time corresponds to T_1 in the high-weight-fraction range in Fig. 14, which follows the predicted scaling with $\dot{\gamma}_c^{-1}$ of the contact relaxation time it takes for particles to separate against viscous drag [28]. An extrapolation of the relaxation time T_1 in Fig. 14 drops below the viscous dissipation time T_N at a weight fraction consistent with that where the normal stress becomes negative during relaxation. This confirms the structural relaxation time is shorter than the viscous dissipation time in the generalized Newtonian regime, and explains the transition from positive to negative normal stress during the transition from steady-state to relaxation. The intermittency of high stresses that makes discontinuous shear thickening intermittent in the low-weight-fraction range for the steady-state viscosity curves of Fig. 2 might also be the result of the structural relaxation time T_1 being comparable to the viscous dissipation time T_N.

If the positive normal stress at high weight fractions ($58.8\% < \phi_{eff} < \phi_c$) is the result of a system spanning network of particle contacts, most of the anomalous features of the shear stress relaxation in the rate-controlled experiments could also be explained. The initially positive shear stress during relaxation was inconsistent with the generalized Newtonian model (see Fig. 10), or any hydrodynamic model in which the suspension continued to flow during relaxation in the direction of initial motion of the plate. If instead a temporary, nearly static structure forms after $t = 0$, as in the case of dynamic shear jamming [31], the built-up strain of the structure structure could continue to apply a stress on the plate opposite the original direction of motion, explaining the positive shear and normal stresses during rate-controlled relaxation. Furthermore, if the local shear stress during relaxation is more dependent on normal stress via a solid-frictional coupling as in steady-state DST rather than on

the local shear rate between particles [20], then there is no longer any expectation that the shear stress should drop quickly to near τ_{min} according to the steady-state $\tau(\dot{\gamma})$ relation in the generalized Newtonian model, as seen in Fig. 7. Instead, the shear stress could remain on the scale of the normal stress, as seen in Figs. 11 and 12.

Finally, the observation that the relaxation time in the high-weight-fraction range ($58.8\% < \phi_{eff} < \phi_c$, $\dot{\gamma}_c^{-1} > 0.54$ s) is independent of the control mode (i.e. stress-controlled or rate-controlled) is inconsistent with the generalized Newtonian model in which the viscosity is intrinsic, or any model where the relaxation is limited by the need to dissipate the angular momentum of the tool, but it is expected if the relaxation is determined by the breakup of the system-spanning structure internal to the suspension.

C. Oscillations

In the high-weight-fraction range of $58.8\% < \phi_{eff} < \phi_c$, ($\dot{\gamma}_c^{-1} > 0.54$ s), we found that the shear rate oscillates in stress-controlled relaxation experiments, as seen in Fig. 8. In particular the oscillation was found in cases where the damping was weak (i.e. the relaxation time T_1 was large compared to the oscillation period). This feature is indicative of elastic energy storage in the system-spanning structure of particles in contact. While the oscillations observed in stress-controlled relaxation experiments could be described by a viscoelastic model with shear modulus $G = 7$ Pa (Sec. V B), such a model would also predict oscillations when applied to rate-controlled measurements, with the only difference being whether or not the tool inertia is included. However, since we did not observe oscillations in the rate control experiments in the same weight fraction range, we can rule out a straightforward viscoelastic extension to the generalized Newtonian model. Therefore, another model is needed to describe these oscillations.

The oscillatory response may also be related to previously observed S-shaped $\tau(\dot{\gamma})$ curves in stress-controlled measurements [32, 33]. In such $\tau(\dot{\gamma})$ curves there is an unstable region of decreasing shear rate with increasing stress, which results in irregular oscillations from a low-stress liquid state to a high-stress solid-like state in steady-state stress-controlled measurements, but not in rate-controlled measurements [32, 33]. Indeed, the initial shear rates in the stress-controlled relaxation measurements in Fig. 8 were much less than $\dot{\gamma}_c$, even though we set the initial shear stress to be greater than τ_{max}, only possible due to the S-shaped $\tau(\dot{\gamma})$ curve. We note that the other stress-controlled measurement in the high weight fraction range at $\phi_{eff} = 59.4\%$ showed no oscillation, but also had $\dot{\gamma}/\dot{\gamma}_c = 21$ for $t < 0$, which would put it back on the stable branch of an S-shaped $\tau(\dot{\gamma})$ curve, where no oscillations would be expected. Thus, the oscillatory behavior observed in our high-weight-fraction range ($58.8\% < \phi_{eff} < \phi_c$) could be due to S-shaped $\tau(\dot{\gamma})$ curves with a shear modulus G for stress-controlled measurements only.

VII. CONCLUSIONS

We showed that using the critical shear rate $\dot{\gamma}_c$ to characterize an effective weight fraction ϕ_{eff} can more precisely characterize material properties near the critical point at the liquid-solid transition ϕ_c with an uncertainty of 0.3% (Fig. 4). This high precision allowed us to distinguish multiple transitions in behavior that are separated by about only 1% in weight fraction, something that could not have been done with larger uncertainties in weight fraction ϕ_{wt} directly measured by weight due to the suspensions' tendency to absorb different amounts of water from the atmosphere at different temperature and humidity conditions. This conversion to ϕ_{eff} (Fig. 3) can also be used to compare experiments done in other laboratories or under different temperature and humidity conditions on a consistent ϕ_{eff} scale at our reference temperature and humidity environment, something which has not been achieved before without a measurement of ϕ_c due to the sensitivity of the weight fraction of suspensions like cornstarch and water to temperature and humidity. We caution the parameter values we obtained may still only apply for measurements at the same gap size, as the critical shear rate has been known to vary with gap size [23].

Transient measurements of stress relaxation over time revealed that DST fluids exhibit relaxation behavior consistent with a generalized Newtonian model in which the function $\tau(\dot{\gamma})$ measured in steady state could describe transient measurements of shear stress and shear rate during relaxation only for $\phi_{eff} < 58.8 \pm 0.3$ %. In this low weight-fraction range, we found an initially quick relaxation – though not well-resolved – which was consistent with relaxation at viscosity η_{max}, approximately the viscosity of the initial steady-state before relaxation. Once the shear rate or stress dropped below about the onset of shear thickening [$(2.2 \pm 0.5)\dot{\gamma}_c$ for stress-controlled experiments (Fig. 8), or $(1.6 \pm 0.9)\tau_{min}$ for rate-controlled experiments (Fig. 13)], we observed an exponential relaxation with transient viscosity η_t matching η_{min}, approximately the viscosity at shear rates and stresses below the onset of shear thickening.

However, for $58.8\% < \phi_{eff} < \phi_c$ ($\dot{\gamma}_c^{-1} > 0.54$ s), we found the relaxation behavior was inconsistent with the generalized Newtonian model. We found the suspensions to relax without the initial fast relaxation to τ_{min} in rate-controlled experiments, or $\dot{\gamma}_c$ in stress-controlled experiments, predicted by the generalized Newtonian model (Figs. 8, 13). In stress-controlled measurements, we also observed the shear rate initially became negative during relaxation, and oscillate in some cases. These features can be described by a shear modulus G that applies only in stress-controlled relaxation due to the history-dependence of S-shaped $\tau(\dot{\gamma})$ curves [32, 33]. In

rate-controlled experiments, for $59.8\% \leq \phi_{eff} < \phi_c$ ($\dot{\gamma}_c^{-1} \geq 3.4$ s), we observed two exponential ranges could be fit to the shear stress relaxation in Fig. 13a, in contrast to the single exponential range observed elsewhere. The scaling of T_1 agrees with a prediction of the contact relaxation time for particles to separate [28], while the physical origin of the second, faster relaxation time is unknown.

For $58.8\% < \phi_{eff} < \phi_c$, ($\dot{\gamma}_c^{-1} > 0.54$ s), the transient viscosity values were found to decrease with ϕ_{eff}, in contrast to the trend of increasing steady-state viscosity η_{min} with ϕ_{eff}. The discrepancy was measured to be as large as 4 orders of magnitude. The extrapolated trends in Fig. 9 suggests the difference may diverge in the limit as $\phi_{eff} \to \phi_c$. In this limit, the generalized Newtonian prediction approaches 0, while the fit of T_1 goes to infinity.

For $58.8\% < \phi_{eff} < \phi_c$ ($\dot{\gamma}_c^{-1} > 0.54$ s) we also found that the relaxation time T_1 was a more consistent material property than viscosity when comparing stress- and rate-controlled measurements (Fig. 14), corresponding to a relaxation time of an internal structure. In contrast, in the generalized Newtonian model, viscosity is the intrinsic property and relaxation time is dependent on flow control. Relaxation times are still expected to scale with system size in the high-weight-fraction regime, which was not investigated here.

We found a one-to-one correspondence between the weight fractions at which the steady-state viscosity curves were consistently discontinuous in rate-controlled measurements, with a nearly constant stress for $\tau > \tau_{max}$ (Fig. 2), and those at which the relaxation was inconsistent with the generalized Newtonian behavior. This indicates a connection between the slow relaxation and discontinuous shear thickening. We also found a one-to-one correspondence between positive normal stress during relaxation and inconsistency of the relaxation with the generalized Newtonian model (Figs. 7, 11, 12), suggesting the continued existence of a system-spanning network of solid particle contacts during relaxation. On the other hand, normal stresses which started out positive in the steady state became negative during relaxation at low weight fractions [$\phi_{eff} < 58.8\%$ ($\dot{\gamma}_c^{-1} < 0.54$ s)] may be a result of the structural relaxation time T_1 becomimg shorter than the viscous relaxation time T_N (Fig. 14). The persistence of this solid-like structure at high weight fractions [$58.8\% < \phi_{eff} < \phi_c$ ($\dot{\gamma}_c^{-1} > 0.54$ s)] accounts for many of the features in the relaxation behavior that are inconsistent with the generalized Newtonian model, including the energy storage (Fig. 7), the lack of initial fast relaxation while the shear stress remains coupled to the normal stress via frictional contacts (Figs. 6 and 10), and the lack of negative stress in rate-controlled relaxation due to the evolution of the shear profile (Fig. 10).

Disagreement with the generalized Newtonian model at high packing fractions indicates a failure in the assumptions used – in particular the assumption that the steady-state $\tau(\dot{\gamma})$ relation can fully describe the transient flow. While the solutions also assume a laminar flow, for a low-Reynolds-number flow like ours in a parallel plate rheometer, a non-laminar flow can only result in a mild discrepancy in which the reported steady-state η_{min} could be an overestimate by as much as 1/3 of the yield stress, putting an upper bound on this correction of 33%, which does not come close to the 4-orders-of-magnitude discrepancy we found with the generalized Newtonian model at the highest ϕ_{eff}. The failure of a $\tau(\dot{\gamma})$ relation at the local level was previously known due to the dominance of a frictional term in the constitutive relation where shear stress is proportional to normal stress [20, 23, 34]. However, the dominance of the frictional term in $\tau(\dot{\gamma})$ occurs over a much wider range of packing fractions, including the continuous shear thickening range [20, 35], so the dominance of the frictional term in the constitutive relation does not in itself predict the failure of the generalized Newtonian model. The failure to predict the relaxation time from the generalized Newtonian model leads to the surprising conclusion that the relaxation is not controlled by the dissipative terms in the constitutive relation. This discrepancy can be explained once the contact relaxation time is considered, which is larger than the dissipative relaxation time in the same packing fraction range the generalized Newtonian model fails, so that the contact relaxation only slows the overall relaxation at the higher packing fractions. Thus, to account for the full range of relaxation behavior we observed requires the addition of terms to the generalized Newtonian model including not only the frictional term that is needed for steady state, but also the shear modulus G, as well as the structural relaxation time T_1, and relaxation time of unknown origin T_2.

A nonzero relaxation time in the limit of large weight fractions may have important consequences for the phenomena exhibited by DST fluids. For example, after an impacting object stops, if the relaxation followed a generalized Newtonian model, expected relaxation times would be less than 0.01 s in the discontinuous shear thickening range, where the response of cornstarch and water to impact is strongest [13]. This would be far too short for a pool of cornstarch and water to support a load like a solid long enough for a person to step on it while they run across (a duration of typically 0.15 s) [13, 36]. In contrast, we measured relaxation times on the order of 1 s at the highest weight fractions below ϕ_c, long enough to support a running person. Other phenomena like the velocity oscillations of a sinking sphere [7] or rolling a sphere on the surface of the suspension [17] would end much too fast to be observable by the naked eye based on the generalized Newtonian model. For such phenomena to be noticeable as dynamic with the naked eye requires a timescale on the order of seconds, which is in the range of what we find at large weight fractions. How to specifically model such phenomena with a constitutive relation that includes a relaxation time, for example using the model of Ozgen et al. [16] is left open for future work.

ACKNOWLEDGMENTS

We would like to thank Heinrich Jaeger for valuable discussions and suggestions. This work was supported by the National Science Foundation under grant DMR-1410157.

[1] Y. S. Lee, E. D. Wetzel, and N.J Wagner, "The ballistic impact characteristics of kevlar-woven fabrics impregnated with a colloidal shear thickening fluid," J. Materials Sci. **38**, 2825 (2003).

[2] http://www.d3o.com/,.

[3] H. A. Barnes, "Shear-thickening ("dilatancy") in suspensions of nonaggregating solid particles dispersed in newtonian liquids," J. Rheology **33**, 329 (1989).

[4] "https://www.youtube.com/watch?v=jks1ymq73oc, http://www.wimp.com/pool-filled-with-non-newtonian-fluid-cornstarch-and-water/," (2008).

[5] E. Brown and H. M. Jaeger, "Shear thickening in concentrated suspensions: phenomenology, mechanisms, and relations to jamming," Reports on Progress in Physics **77**, 046602–1–23 (2014).

[6] F. S. Merkt, R. D. Deegan, D. I. Goldman, E. C. Rericha, and H. L. Swinney, "Persistent holes in a fluid," Phys. Rev. Lett. **92**, 184501 (2004).

[7] S. von Kann, J. H. Snoeijer, D. Lohse, and D. van der Meer, "Non-monotonic settling of a sphere in a cornstarch suspension," Phys. Rev. E **84**, 060401 (2011).

[8] E. Brown and H. M. Jaeger, "Dynamic jamming point for shear thickening suspensions," Phys. Rev. Lett. **103**, 086001 (2009).

[9] E. Brown, H. Zhang, N. A. Forman, B. W. Maynor, D. E. Betts, J. M. DeSimone, and H. M. Jaeger, "Shear thickening and jamming in densely packed suspensions of different particle shapes," Phys. Rev. E **84**, 031408–1–11 (2011).

[10] N.J. Wagner and J. F. Brady, "Shear thickening in colloidal dispersions," Phys. Today, Oct. 2009 , 27–32 (2009).

[11] S. R. Waitukaitis and H. M. Jaeger, "Impact-activated solidification of dense suspensions via dynamic jamming fronts," Nature **487**, 205–209 (2012).

[12] I. R. Peters and H. M. Jaeger, "Quasi-2d dynamic jamming in cornstarch suspensions: visualization and force measurements," Soft Matter **10**, 6574–6570 (2014).

[13] R. Maharjan, S. Mukhopadhyay, B. Allen, T. Storz, and E. Brown, "Constitutive relation of the system-spanning dynamically jammed region in response to impact of cornstarch and water suspensions," arXiv:1407.0719 (2017).

[14] R. D. Deegan, "Stress hysteresis as the cause of persistent holes in particulate suspensions," Phys. Rev. E **81**, 036319 (2010).

[15] S. von Kann, J. H. Snoeijer, and D. van der Meer, "Velocity oscillations and stop-go cycles: The trajectory of an object settling in a cornstarch suspension," Phys. Rev. E **87**, 042301 (2013).

[16] O. Ozgen, E. Brown, and M. Kallman, "Simulating the dynamic behavior of shear thickening fluids," arXiv:1510.09069 (2015).

[17] "https://www.youtube.com/watch?v=8seb0nhx5tu," (2009).

[18] Y. S. Lee and N.J Wagner, "Dynamic properties of shear thickening colloidal suspensions," Rheol. Acta **42**, 199–208 (2003).

[19] S. R. Raghavan and S. A. Khan, "Shear-thickening response of fumed silica suspensions under steady and oscillatory shear," J. Colloid and Interface Science **185**, 57–67 (1997).

[20] E. Brown and H. Jaeger, "The role of dilation and confining stress in shear thickening of dense suspensions," J. Rheology **56**, 875–923 (2012).

[21] Neil Y. C. Lin, Ben M. Guy, Michiel Hermes, Chris Ness, Jin Sun, Wilson C. K. Poon, and Itai Cohen, "Hydrodynamic and contact contributions to shear thickening in colloidal suspensions," Physical Review Letters **115**, 228304 (2015).

[22] D. Lootens, H. Van Damme, and P. Hébraud, "Giant stress fluctuations at the jamming transition," Phys. Rev. Lett. **90**, 178301 (2003).

[23] A. Fall, F. Bertrand, G. Ovarlez, and B. Bonn, "Shear thickening of cornstarch suspensions," J. Rheology **56**, 575–591 (2012).

[24] Jan Mewis and Norman J. Wagner, *Colloidal Suspension Rheology* (Cambridge University Press, 2012).

[25] Frank M. White, *Fluid Mechanics*, 7th ed. (McGraw-Hill, 2009).

[26] D. Lootens, H. vanDamme, Y. Hémar, and P. Hébraud, "Dilatant flow of concentrated suspensions of rough particles," Phys. Rev. Lett. **95**, 268302 (2005).

[27] R. Seto, R. Mari, J. F. Morris, and M. M. Denn, "Discontinuous shear thickening of frictional hard-sphere suspensions," Phys. Rev. Lett. **111**, 218301 (2013).

[28] J. R. Melrose and R. C. Ball, "Continuous shear thickening transitions in model concentrated colloids – the role of interparticle forces," J. Rheology **48**, 937 (2004).

[29] J. F. Brady and J. F. Morris, "Microstructure of strongly sheared suspensions and its impact on rheology and diffusion," J. Fluid Mech. **348**, 103–139 (1997).

[30] M. Wyart and M. E. Cates, "Discontinuous shear thickening without inertia in dense non-brownian suspensions," Phys. Rev. Lett. **112**, 098302 (2014).

[31] I. R. Peters, S. Majumdar, and H. M. Jaeger, "Direct observation of dynamic shear jamming in dense suspensions," Nature **532**, 214–217 (2016).

[32] Hiizu Nakanishi, S. Nagahiro, and Namiko Mitarai, "Fluid dynamics of dilatant fluids," Phys. Rev. E **85**, 011401 (2012).

[33] Michiel Hermes, Ben M. Guy, Wilson C. K. Poon, Guilhem Poy, Michael E. Cates, and Matthieu Wyart, "Unsteady flow and particle migration in dense, nonbrownian suspensions," Journal of Rheology **60**, 905–916 (2016).

[34] A. Fall, A. Lemaitre, and G. Ovarlez, "Discontinuous shear thickening in cornstarch suspensions," EPJ Web of Conference: Powders and Grains 2017 **140**, 09001 (2017).

[35] John R. Royer, Daniel L. Blair, and Steven D. Hudson, "Rheological signature of frictional interactions in shear thickening suspensions," Physical Review Letters **116** (2016).

[36] Peter G. Weyand, Deborah B. Sternlight, Matthew J. Bellizzi, and Seth Wright, "Faster top running speeds are achieved with greater ground forces not more rapid leg movements," J. Applied Physiology **89**, 1991–1999 (2000).